Inorganic Chemistry Communications 143 (2022) 109779

Contents lists available at ScienceDirect

Inorganic Chemistry Communications

journal homepage: www.elsevier.com/locate/inoche

Short communication

Dual inhibition of *S. aureus TyrRS* and *S. aureus gyrase* by two 4-amino-4′-acetyldiphenyl sulfide-based Schiff bases: Structural features, DFT study, *Hirshfeld* surface analysis and molecular docking

Soumia Kadri [a], Amani Direm [b,*], Hamza Athmani [b], Brahim El Bali [c], Cemal Parlak [d], Rabihe Hebbachi [a]

[a] *Environmental and Structural Molecular Chemistry Research Unit, Faculty of Exact Sciences, Department of Chemistry, University of Mentouri Brothers, Constantine 1, Constantine 25.000, Algeria*
[b] *Laboratory of Structures, Properties and Interatomic Interactions LASPI²A, Department of Matter Sciences, Faculty of Sciences and Technology, Abbes Laghrour University, Khenchela 40.000, Algeria*
[c] *Independent Scientist, Marrakech, Morocco*
[d] *Department of Physics, Science Faculty, Ege University, Izmir 35100, Turkey*

ARTICLE INFO

Keywords:
Schiff bases
Staphylococcus *aureus*
Antimicrobial resistance
Dual inhibition
DFT
Hirshfeld surface analysis
Molecular docking

ABSTRACT

Two 4-amino-4′-acetyldiphenyl sulfide-based Schiff bases, namely 1-[4-({4-[(E)-(2-hydroxynaphthalen-1-yl) methylideneamino]phenyl}sulfanyl)-phenyl]ethanone (**I**) and (E)-1-[4-({4-[(4-methoxybenzylidene)amino] phenyl}-sulfanyl)phenyl]ethan-1-one (**II**) were structurally studied. They crystallize respectively in the monoclinic *Cc* and the triclinic *P*1 space groups, with the respective cell parameters: [10.695(3) Å, 44.458(14) Å, 4.4437(11) Å, 99.004(9)°] and [5.7708(2) Å, 8.0867(3) Å, 19.6929(8) Å, 81.844(2)°, 86.664(3)°, 85.662(3)°]. The asymmetric units of (**I**) and (**II**) are composed of one molecule and two crystallographically independent molecules, respectively. Their molecular structures were optimized by the density functional theory and correlated correspondingly to the crystal structures. Moreover, the IR vibration modes were assigned to the calculated wavenumbers, the *Mulliken* atomic charges obtained and the frontier molecular orbitals evaluated. The hydrogen bonding and the non-classical intermolecular interactions within the two frameworks were investigated using *Hirshfeld* surface analysis which indicated the presence of C—H…H—C, C—H···π, C—H···O, C—H···N, C—H···S and π···*lp* interactions as well as π···π stacking. Additionally, in order to understand the interacting binding sites of the two molecules with the bacterial *S. aureus* protein receptors, the studied compounds were *in silico* evaluated by molecular docking against tyrosyl-tRNA synthetase **1JIJ** and topoisomerase II DNA gyrase **2XCT** enzymes. The results revealed consequently potent antimicrobial efficacy through the formed hydrogen bonds, hydrophobic contacts, π-cation interactions and π…π stacking.

1. Introduction

Gram-positive methicillin-resistant Staphylococcus aureus (MRSA) is one of the most common antibiotic-resistant bacteria. It causes life-threatening bloodstream, surgical-site infections and pneumonia. This class of infection-causing bacteria cannot be controlled or killed by antibiotics and it is instead able to survive and even multiply in the presence of an antibiotic [1–6]. Despite the ongoing pharmaceutical research undertaken in order to respond to the clinical need to develop new antibiotics, the antimicrobial resistance (AMR) continues to be challenging and the spread of antibiotic-resistant bacteria poses a substantial threat to public health worldwide [7–10]. Therefore, a growing clinical need for the ability to continuously develop new potent antimicrobial compounds is to be urgently considered to fight clinical diseases and to equipotently inhibit multiple bacterial targets [11–13].

In fact, tyrosyl-tRNA synthetase (TyrRS) belongs to the aminoacyl-tRNA synthetases which play a key role in the catalysis of the amino acids' condensation with their respective tRNA to form charged tRNAs [14]. In addition, the inhibition of these enzymes affects the cell growth by altering the protein biosynthesis process. Thus, TyrRS represents an attractive target enzyme to develop new potent antibacterial agents [15,16]. On the other hand, type II DNA topoisomerases are vital

* Corresponding author.
E-mail addresses: direm.amani@univ-khenchela.dz, amani_direm@yahoo.fr (A. Direm).

https://doi.org/10.1016/j.inoche.2022.109779
Received 12 May 2022; Received in revised form 24 June 2022; Accepted 17 July 2022
Available online 19 July 2022

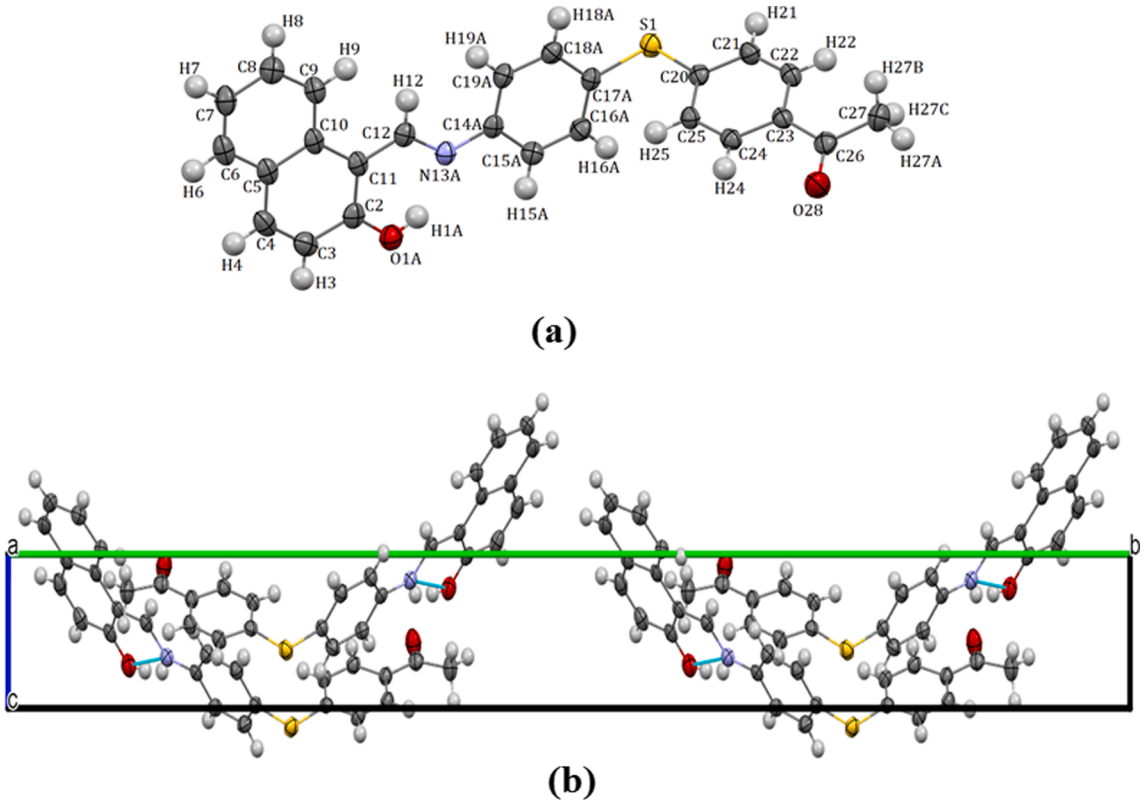

Fig. 1. **(a)** Atomic labeling of the asymmetric unit of compound (**I**), **(b)** view of its packing along the *a*-axis.

enzymes which support the DNA replication, chromosome decatenation, condensation and other DNA-associated processes. The function of topoisomerases II DNA gyrase is essential for the negative supercoiling of DNA at the expense of ATP hydrolysis. Being highly conserved enzymes with known crystal structures and well-described mechanism, they are hence recognized as well-established antibacterial targets [17–22]. Furthermore, DNA gyrase inhibitors are able to affect the enzyme action at many levels [23].

On the other hand, Schiff bases known also as imines or azomethines represent an important class of naturally occurring and/or synthetic organic molecules that are versatile due to their ability to combine a variety of alkyl or aryl substituents as well as metallic centers. For years, these systems have been greatly attracting the attention of many scientists and inspiring them to design new molecules and to investigate their applications' fields [24]. Accordingly, they are *inter alia* used in catalytic reactions, as *in vivo* photo- or chemodetectors of Al^{3+} ions in biological systems and most commonly in medicine [25]. Therefore, they are well known for their medical applications as antibacterial [26–28], antifungal [29], antiviral [30,31], anti-inflammatory [32], antipyretic, antimalarial [33,34], anticancer [35–39] agents. Additionally, their oxytocin-imitating and inhibiting activity, as well as their human tyrosine phosphatases (PTP1B, TCPTP or SHP-1) selective inhibition were proven [40–42]. Recently, a number of papers reported on Schiff bases evaluated for their *S. aureus* DNA gyrase and/or TyrRS inhibition [43–48].

Consequently, taking the above studies into account, the dual targeting of antibacterial compounds to these two enzymes' classes will reduce the bacteria probability to develop target-based resistance against these actions. To better understand the mechanism of action of antibacterial molecules, we investigate in this study the *in silico* dual antibacterial efficacy of two 4-amino-4′-acetyldiphenyl sulfide Schiff bases, namely 1-[4-({4-[(E)-(2-hydroxynaphthalen-1-yl)methylideneamino]phenyl}sulfanyl)-phenyl]ethanone (**I**) and (E)-1-[4-({4-[(4-methoxybenzylidene) amino]phenyl}- sulfanyl)phenyl]ethan-1-one (**II**), against these enzymes. We studied for the first time their binding modes towards the mentioned enzymes using molecular docking analysis as well as exploring the leading intermolecular interactions and the non-classical contacts within their respective frameworks *via Hirshfeld* surface analysis based on their crystal data. $C_{25}H_{19}NO_2S$ (**I**) and $C_{22}H_{19}NO_2S$ (**II**) crystallize respectively in the monoclinic *Cc* and the triclinic *P*1 space groups [49,50]. Furthermore, in order to gain more insights into the molecular and electronic properties of the studied molecules, and as no such investigation was previously reported, we report herein the optimized structures of both compounds, their frontier molecular orbitals' analysis, their IR vibration modes and the corresponding *Mulliken* charges computed using both ***B3LYP/6-31G(d)*** and ***B3LYP/cc-pvdz*** levels of theory.

2. Materials and methods

2.1. Computational details

Both molecules (**I**) and (**II**) were optimized in the gas phase using the ***B3LYP*** functional in conjunction with the ***6-31G(d)*** and ***cc-pvdz*** basis sets using Gaussian 09 [51]. Furthermore, the vibrational wavenumber calculations were carried out together with the frontier molecular orbitals. Harmonic vibrational wavenumbers of the compounds were scaled by 0.960 for ***B3LYP/6-31G(d)*** and 0.970 for ***B3LYP/cc-pvdz*** methods [52]. To visualize the examined structures, we used GaussView program [53].

2.2. Hirshfeld surface analysis

In order to analyze the intermolecular interactions in the studied organic compounds, their molecular packing were investigated by means of the 2D-Fingerprint plot **FP** and the *Hirshfeld* surface **HS** analyses using CrystalExplorer17.5 program [54]. The **HS** was mapped over d_{norm}, d_e and *shape index* functions, respectively in the range of (−0.216

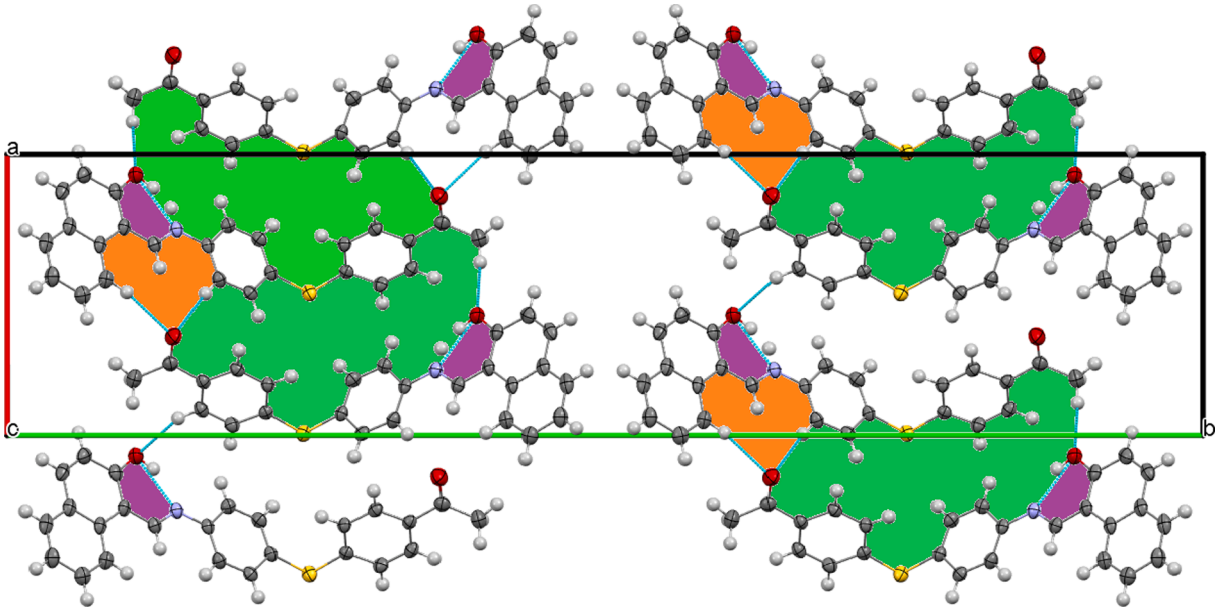

Fig. 2. (*ab*) Crystal structure projection of (**I**) showing the molecules linked through the C—H···O hydrogen bonds, forming $R_2^1(10)$(in orange) and $R_3^3(26)$ (in green) ring motifs. The violet color shows the $S_1^1(6)$ motifs built of the intramolecular H-bonds.

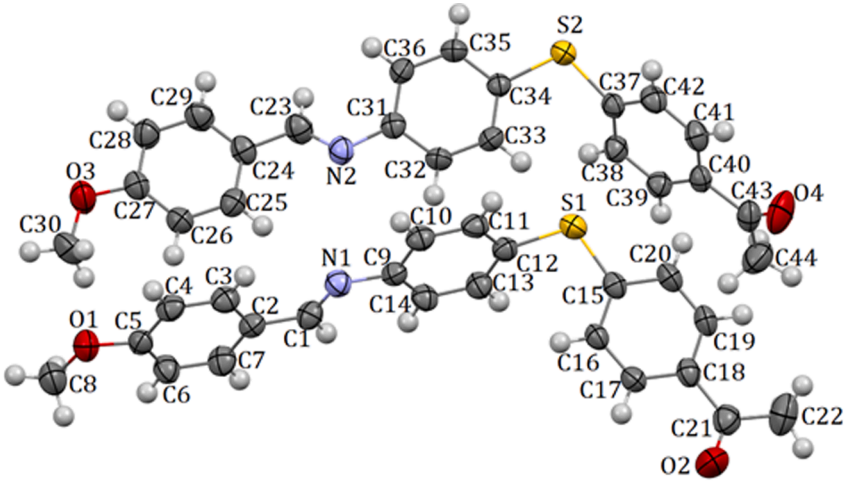

(a)

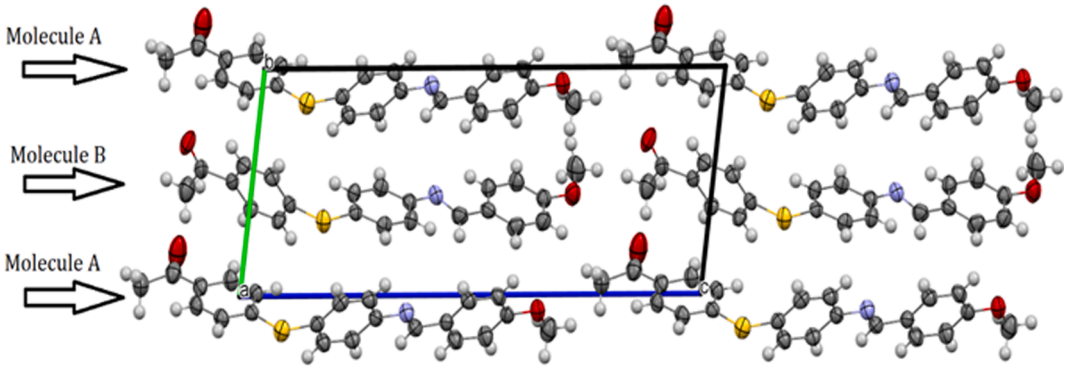

(b)

Fig. 3. (a) Asymmetric unit of (**II**). H atoms labelling have been omitted for clarity sake, **(b)** view of its packing along the *a*-axis, showing the altering chains of molecules **A** and **B**.

Table 1
Experimental and theoretical bond lengths in compounds (**I**) and (**II**).

Bond length (Å)	Exp.	Theoretical		Bond length (Å)	Exp.	Theoretical	
		B3LYP/ 6-31G(d)	*B3LYP/ cc-pvdz*			*B3LYP/ 6-31G(d)*	*B3LYP/ cc-pvdz*
(I)							
O1A—C2	1.277 (4)	1.335	1.331	C14A—C15A	1.393 (5)	1.407	1.409
C2—C3	1.429 (4)	1.420	1.423	C15A—C16A	1.387 (4)	1.392	1.394
C3—C4	1.354 (5)	1.367	1.369	C16A—C17A	1.383 (5)	1.402	1.403
C4—C5	1.437 (5)	1.425	1.428	C18A—C19A	1.389 (4)	1.391	1.393
C5—C6	1.420 (5)	1.417	1.419	S1—C17A	1.780 (3)	1.792	1.797
C6—C7	1.363 (5)	1.378	1.380	S1—C20	1.764 (3)	1.789	1.792
C8—C9	1.380 (5)	1.381	1.383	C20—C21	1.401 (4)	1.402	1.405
C9—C10	1.404 (5)	1.419	1.421	C20—C25	1.394 (4)	1.404	1.406
C10—C11	1.453 (4)	1.449	1.449	C21—C22	1.389 (4)	1.389	1.392
C11—C12	1.404 (4)	1.443	1.444	C22—C23	1.385 (5)	1.403	1.405
C11—C2	1.438 (5)	1.414	1.416	C23—C26	1.489 (4)	1.494	1.497
C12—N13A	1.334 (4)	1.299	1.302	C24—C25	1.378 (4)	1.390	1.393
N13A—C14A	1.407 (4)	1.403	1.405	C26—C27	1.500 (4)	1.521	1.519
dC14A—C19A	1.388 (4)	1.405	1.407	C26—O28	1.232 (4)	1.223	1.222
(II)							
Molecule A							
S1—C15	1.765 (4)	1.789	1.792	C9—C14	1.391 (5)	1.405	1.407
S1—C12	1.776 (4)	1.793	1.797	C10—C11	1.381 (5)	1.391	1.394
O1—C5	1.363 (4)	1.362	1.362	C11—C12	1.381 (5)	1.403	1.404
O1—C8	1.430 (5)	1.425	1.425	C12—C13	1.386 (5)	1.402	1.403
O2—C21	1.210 (5)	1.224	1.223	C13—C14	1.374 (5)	1.392	1.394
N1—C1	1.252 (4)	1.283	1.284	C15—C20	1.389 (5)	1.403	1.405
N1—C9	1.417 (4)	1.402	1.403	C15—C16	1.389 (5)	1.403	1.405
C1—C2	1.459 (5)	1.461	1.463	C16—C17	1.379 (5)	1.389	1.391
C2—C7	1.391 (5)	1.401	1.402	C18—C19	1.387 (5)	1.403	1.405
C2—C3	1.392 (5)	1.410	1.412	C18—C21	1.486 (5)	1.497	1.499
C3—C4	1.369 (5)	1.382	1.384	C19—C20	1.374 (5)	1.392	1.394
C5—C6	1.381 (5)	1.400	1.402	C21—C22	1.498 (6)	1.518	1.515
C6—C7	1.380 (5)	1.394	1.396				
Molecule B							
S2—C37	1.775 (3)	1.789	1.792	C31—C36	1.388 (5)	1.407	1.408
S2—C34	1.779 (3)	1.793	1.798	C32—C33	1.382 (5)	1.389	1.391
O3—C27	1.362 (4)	1.362	1.361	C33—C34	1.382 (5)	1.404	1.405
O3—C30	1.424 (5)	1.425	1.425	C34—C35	1.387 (5)	1.400	1.401
O4—C43	1.207 (5)	1.226	1.225	C35—C36	1.382 (5)	1.394	1.396
N2—C23	1.260 (4)	1.284	1.284	C37—C38	1.385 (5)	1.401	1.403
N2—C31	1.429 (4)	1.404	1.402	C38—C39	1.370 (5)	1.392	1.394
C23—C24	1.464 (5)	1.461	1.463	C39—C40	1.383 (5)	1.403	1.405
C24—C29	1.378 (5)	1.407	1.409	C40—C41	1.386 (5)	1.405	1.407
C24—C25	1.389 (5)	1.404	1.406	C40—C43	1.491 (5)	1.492	1.495
C25—C26	1.391 (5)	1.389	1.392	C41—C42	1.384 (5)	1.387	1.389
C27—C28	1.372 (5)	1.404	1.406	C43—C44	1.485 (6)	1.519	1.517
C28—C29	1.376 (5)	1.386	1.389				

to 3.088 Å), (0.992 to 3.670 Å), (−1.000 to 1.000 Å) for (**I**) and (−0.101 to 1.349 Å), (1.041 to 2.419 Å), (−1.000 to 1.000 Å) for (**II**), in order to emphasize the contacts and their leading interactions towards the stability of the crystal packing.

2.3. Molecular docking

The *in silico* studies were carried out by performing a molecular docking simulation with the AutoDock4.2 software and AutoDock Tools ADT [55]. The X-ray crystal structures of *S. aureus* tyrosyl-tRNA synthetase and *S. aureus* topoisomerase II DNA gyrase were downloaded from the RCSB protein data bank [56] with respectively the PDB ID: **1JIJ** [57] and **2XCT** [58]. The ligands and receptors structures were then treated by removing the co-crystallised inhibitors and co-factors. The non-polar hydrogens of the structures were merged in ADT [55] and the PDBQT format files were prepared by considering the ligands' rotatable bonds and assigning the Gasteiger and the Kollman charges to the related structures. Furthermore, the interacting residues involved in the binding pockets of the resulting docked complexes were evaluated and analyzed using Chimera software [59].

3. Results and discussion

3.1. Structural description

The asymmetric unit of (**I**) is drawn in Fig. 1.a, its crystal structure can be described as *head*-to-*head* and *foot*-to-*foot* waves extending along the *b*-axis (Fig. 1.b).

The neighboring molecules are linked through C—H···O hydrogen bonds giving rise to infinite chains running along the *a*-axis. Furthermore, the asymmetric unit is connected to four neighboring molecules through four intermolecular C—H···O interactions and an intramolecular O—H···N interaction. As a result, the intramolecular O1—H1A···N13A hydrogen bond constitutes a $S_1^1(6)$ ring motif, while the C—H···O hydrogen bonds form two $R_2^1(10)$ and $R_3^3(26)$ ring motif in the (*ab*) plane [60] (Fig. 2).

The asymmetric unit of compound (**II**) given in Fig. 3.a is formed by two crystallographically independent molecules including 4-methoxybenzylidene moieties compared to compound (**I**) which showed 2-*oxo*-naphthalene moieties in the same position. In (**II**), the crystallographically independent molecules; molecule **A** (C1-C22) and molecule **B** (C23-C44), form together alternating chains which extend infinitely parallel to the [0 0 1] direction (Fig. 3.b). The two molecules' rings are inclined to one another by 67.60° for 4-methoxybenzylidene parts and

Table 2
Experimental and theoretical bond angles in (**I**) and (**II**).

Bond angles (°)	Exp.	Theoretical		Bond angles (°)	Exp.	Theoretical	
		B3LYP/ 6-31G(d)	*B3LYP/ cc-pvdz*			*B3LYP/ 6-31G(d)*	*B3LYP/ cc-pvdz*
(**I**)							
O1A—C2—C3	119.1 (3)	116.40	116.91	C17A—C16A—C15A	120.2 (3)	120.43	120.41
O1A—C2—C11	123.1 (3)	122.84	122.59	C18A—C19A—C14A	119.4 (3)	120.64	120.67
C2—C11—C10	120.4 (3)	119.06	119.29	C20—S1—C17A	104.88 (15)	104.33	104.11
C3—C4—C5	121.5 (3)	121.71	121.73	C21—C20—S1	116.1 (2)	124.31	124.39
C4—C3—C2	122.1 (3)	120.20	120.29	C22—C21—C20	120.5 (3)	119.88	119.85
C6—C5—C4	120.6 (3)	120.67	120.80	C22—C23—C26	122.6 (3)	118.48	118.40
C7—C6—C5	121.3 (3)	121.11	121.11	C23—C22—C21	120.9 (3)	121.30	121.37
C8—C9—C10	121.4 (3)	121.48	121.45	C23—C26—C27	119.3 (3)	118.83	118.76
C9—C10—C11	123.6 (3)	123.77	123.68	C24—C25—C20	120.6 (3)	120.22	120.23
C12—C11—C2	119.0 (3)	119.41	119.02	C25—C20—S1	125.2 (2)	116.29	116.23
N13A—C12—C11	122.7 (3)	122.71	122.37	O28—C26—C23	120.2 (3)	120.79	120.66
(**II**)							
Molecule A							
C15—S1—C12	105.80 (17)	104.11	104.00	C11—C12—S1	118.3 (3)	120.79	120.76
C5—O1—C8	118.5 (3)	118.38	118.36	C13—C12—S1	122.2 (3)	119.74	119.70
C1—N1—C9	121.9 (3)	120.16	120.14	C14—C13—C12	120.4 (3)	120.35	120.31
N1—C1—C2	122.5 (3)	122.94	122.71	C13—C14—C9	120.7 (3)	120.74	120.77
C7—C2—C1	120.8 (3)	119.74	119.88	C20—C15—S1	115.1 (3)	116.82	116.73
C3—C2—C1	121.1 (3)	121.83	121.72	C16—C15—S1	125.5 (3)	123.66	123.78
C4—C3—C2	120.6 (4)	120.67	120.67	C17—C16—C15	119.7 (3)	119.83	119.80
O1—C5—C6	124.7 (4)	124.59	124.69	C19—C18—C21	122.5 (3)	123.02	123.11
C7—C6—C5	119.2 (4)	119.24	119.31	C20—C19—C18	121.8 (3)	120.72	120.76
C6—C7—C2	121.6 (4)	121.55	121.55	C19—C20—C15	119.9 (4)	120.26	120.27
C14—C9—N1	126.0 (3)	117.83	118.03	O2—C21—C18	120.4 (4)	120.39	120.26
C12—C11—C10	120.3 (3)	120.37	120.36	C18—C21—C22	119.5 (4)	118.83	118.76
Molecule B							
C37—S2—C34	105.96 (16)	103.32	103.13	C33—C34—S2	125.6 (3)	120.41	120.34
C27—O3—C30	118.7 (3)	118.53	118.51	C35—C34—S2	114.7 (3)	120.18	120.18
C23—N2—C31	119.6 (3)	120.30	120.27	C36—C35—C34	120.0 (4)	120.42	120.40
N2—C23—C24	123.6 (4)	122.93	122.70	C35—C36—C31	120.9 (3)	120.48	120.50
C29—C24—C23	119.2 (4)	119.89	120.02	C38—C37—S2	122.8 (3)	123.55	123.61
C25—C24—C23	122.6 (4)	121.69	121.60	C39—C38—C37	120.1 (3)	119.99	119.98
C24—C25—C26	120.9 (4)	121.17	121.21	C38—C39—C40	121.7 (3)	121.09	121.13
O3—C27—C28	114.8 (4)	115.68	115.71	C39—C40—C43	123.4 (3)	122.83	122.91
C27—C28—C29	120.3 (4)	119.87	119.97	C41—C40—C43	118.7 (3)	118.76	118.72
C28—C29—C24	121.4 (4)	121.05	121.03	C42—C41—C40	121.0 (3)	120.97	121.00
C36—C31—N2	125.3 (3)	123.88	123.94	O4—C43—C44	120.1 (4)	120.56	120.83
C34—C33—C32	120.0 (3)	120.24	120.20	O4—C43—C40	120.3 (4)	120.54	120.36

by 69.57° for 1-{4-[(4-Aminophenyl)sulfanyl]phenyl}ethan-1-one parts. The geometric parameters C—C bonds and C—C—C bond angles show similarity with compound (**I**). Moreover, the sulfur atoms form C—S—C angle of respectively 105.80(17)° and 105.99(16)° in molecules **A** and **B**, which are comparable to the corresponding angle observed in compound (**I**). Whereas, the C—N—C angles being respectively 121.9 (3)° and 119.6(3)° in molecule **A** and **B** are slightly shorter than the corresponding one in compound (**I**).

Compound (**I**) can be split in two parts, namely: 4-acetylphenylsulfanyl- which belongs to a plane as well as the fragments phenyl-aminomethyl- and 2-oxo-naphthalene laying on another plane. The dihedral angle between the two planes is found to be 70.942(87)°. Due to steric effect between the above defined entities, the molecules stack in the *a*-direction. As for compound (**II**), it could be divided into the fragments: phenylethan-1-one which belongs to a plane as well as 4-methoxybenzylidene- and 4-aminophenylsulfanyl- resting together in another plane, with (C10, C11) and (C13, C14) being up and down this plane. The resulting dihedral angle built between the two planes is of 63.759(1 0 3)°. Differently from compound (**I**), the steric effect seems to have no influence in the structure of (**II**).

3.2. Molecular geometry

The geometric parameters of the optimized structures computed for the studied compounds are depicted in Tables 1 and 2. For (**I**), the experimental bond lengths are in the range [1.232 (4), 1.780 (3)] Å with a mean value of about 1.419 Å (Table 1). The corresponding optimized values computed at the ***B3LYP/6-31G(d)*** and ***B3LYP/cc-pvdz*** levels are respectively in the range [1.223, 1.792] Å and [1.222, 1.797] Å, with average bond lengths of 1.427 Å and 1.429 Å, respectively. These values are in a good agreement with the experimental ones, with a maximum deviation value of 0.058 Å and 0.054 Å observed for the bond O1A—C2 estimated using ***B3LYP/6-31G(d)*** and ***B3LYP/cc-pvdz***, respectively. As for the experimental bond angles, they vary from 104.88 (15)° to 125.2 (2)° (Table 2) with a mean value of 120.21°. The optimized ones were found to vary from 104.33° to 124.31° for ***B3LYP/6-31G(d)*** and from 104.11° to 124.39° for ***B3LYP/cc-pvdz***, which show correspondingly mean values of 118.68° and 119.74°, and maximum deviation values of 8.91° and 8.97° observed for the bond angle C25—C20—S1.

For compound (**II**), the experimental bond lengths vary in the ranges [1.210 (5), 1.776 (4)] Å and [1.207 (5), 1.779 (3)] Å respectively for molecules **A** and **B**, with the same mean value of 1.416 Å. However, the theoretical ones computed with ***B3LYP/6-31G(d)*** and ***B3LYP/cc-pvdz*** are respectively in the range [1.224, 1.793] Å, [1.223, 1.797] Å for **A** and [1.226, 1.793] Å, [1.225, 1.798] Å for **B**. Thus, the bond lengths maximum deviations are about 0.031 Å and 0.029 Å observed for N1—C1 (molecule **A**) and C24—C29 (molecule **B**) estimated using ***B3LYP/6-31G(d)*** and are found to be 0.032 Å and 0.031 Å related respectively to the same bonds computed using ***B3LYP/cc-pvdz***. Furthermore, the experimental bond angles are varying from 105.80 (17)° to 126.0 (3)° for **A** and from 105.96 (16)° to 125.3 (3)° for **B**. The corresponding values obtained using ***B3LYP/6-31G(d)*** are respectively [104.11, 124.59]° and [103.32, 123.88]°, with mean values of 119.86° and 119.93°. While, those computed with the ***B3LYP/cc-pvdz*** method

Table 3
Calculated IR wavenumbers (cm^{-1}) and their assigned vibration modes in (**I**) and (**II**).

B3LYP/6-31G(d)		*B3LYP/cc-pvdz*		Assigned vibration mode
Frequency	I_{IR}	**Frequency**	I_{IR}	
(I)				
3090.41	20.72	3112.38	16.10	ν_{asym} CH
3081.18	39.52	3102.97	31.62	ν_{asym} CH
3042.37	14.96	3060.25	13.18	ν_{asym} CH_3
2992.62	8.5	3005.10	8.63	ν_{asym} CH + ν_{asym} OH
2911.55	529.19	2835.07	651.91	ν_{asym} OH
1701.94	172.59	1710.14	174.45	ν_{asym} C═O + ν_{asym} C═C + δ_{asym} HCH + δ_{asym} HCC
1613.17	220.04	1624.45	221.26	ν_{asym} C═N + ν_{asym} C═C + δ_{asym} HOC + δ_{asym} CNC + δ_{asym} HCC
1603.38	69.96	1611.79	54.14	ν_{asym} C═N + ν_{asym} C═C + δ_{asym} HOC + δ_{asym} CNC + δ_{asym} HCC
1591.39	25.93	1602.43	45.14	ν_{asym} C═C + δ_{asym} HOC + δ_{asym} CNC + δ_{asym} CCC + δ_{asym} HCC
1557.49	562.29	1564.95	616.97	ν_{asym} C═C + δ_{asym} HOC + δ_{asym} CNC + δ_{asym} CCC + δ_{asym} HCC
1539.51	14.67	1553.29	15.50	δ_{asym} CSC + δ_{asym} HOC + δ_{sym} CNC + δ_{asym} HCC
1448.03	9.16	1406.82	8.08	δ_{asym} CH_3
(II)				
3084.09	12.41	3127.41	10.03	ν_{asym} CH
3037.77	16.29	3055.63	14.84	ν_{asym} CH_3
3036.07	51.42	3048.04	41.19	ν_{asym} CH_3
2989.21	16.85	3001.36	18.26	ν_{sym} CH_3
2985.67	37.03	2997.49	32.89	ν_{sym} CH_3
2905.06	37.61	2926.31	65.61	ν_{asym} CH
2899.70	36.85	2923.62	55.72	ν_{asym} CH
1697.69	143.82	1704.48	150.43	ν_{asym} C═O + ν_{asym} C═C + δ_{asym} HCH + δ_{asym} HCC
1685.19	233.53	1691.17	234.13	ν_{asym} C═O + ν_{asym} C═C + δ_{asym} HCH + δ_{asym} HCC
1602.26	357.61	1644.33	234.33	ν_{asym} C═N + ν_{asym} C═C + δ_{asym} CNC + δ_{asym} CCC + δ_{asym} HCC
1598.21	100.04	1642.76	29.26	ν_{asym} C═N + ν_{asym} C═C + δ_{asym} CNC + δ_{asym} CCC + δ_{asym} HCC
1581.76	447.62	1611.66	350.88	ν_{asym} C═O + ν_{asym} C═C + δ_{asym} CCO + δ_{asym} CCC + δ_{asym} HCC
1559.91	16.05	1553.94	16.21	δ_{asym} CSC + δ_{sym} CNC + δ_{asym} HCC
1558.70	37.20	1552.53	39.26	δ_{asym} CSC + δ_{sym} CNC + δ_{asym} HCC
1463.47	14.89	1434.97	20.98	δ_{asym} CH_3
1459.56	11.59	1431.73	23.19	δ_{asym} CH_3

are [104.00, 124.69]° and [103.13, 123.94]°, respectively, and their associated mean values are 119.85° and 119.93°. Therefore, it is found that the maximum deviation values of the bond angles are 8.17° (**A**) and 5.48° (**B**) obtained by the ***B3LYP/6-31G(d)*** level, whereas the corresponding values are 7.97° (**A**) and 5.48° (**B**) for the ***B3LYP/cc-pvdz*** level. These values associated to the angles C14—C9—N1 (molecule **A**) and C35—C34—S2 (molecule **B**) are not quite significant.

Additionally, by considering the relative deviation Δ for a geometric parameter *X* expressed as the percentage relation given below [61], we found that the overall average deviations, of the computed geometric parameters from the experimental ones given in Tables 1 and 2, are found to be respectively 1.12 %, 1.15 % at the ***B3LYP/6-31G(d)***, ***B3LYP/cc-pvdz*** levels for (**I**) and 1.06 %, 1.15 % at the mentioned levels for (**II**). The obtained values indicate a very good agreement between the discussed results and hence the calculations reproduce well the crystallographic structures of both studied compounds.

$$\Delta = \frac{\left|X_{theo} - X_{exp}\right|}{X_{exp}} \text{x} 100$$

With X_{theo} and X_{exp} being respectively the theoretical and the experimental values of the quantity *X*.

Table 4
Mulliken atomic charges (a.u) in compounds (**I**) and (**II**).

Atoms	B3LYP/6-31G(d)	B3LYP/cc-pvdz	Atoms	B3LYP/6–31G(d)	B3LYP/cc-pvdz
(I)					
O1A	−0.600807	−0.172203	C22	−0.111691	0.071110
C2	0.320414	0.030395	C21	−0.135775	0.083013
C3	−0.135538	0.080509	C26	0.358353	0.016893
C4	−0.129449	0.054125	C27	−0.518487	0.026007
C5	0.093091	0.006588	O28	−0.467709	−0.207758
C6	−0.164757	0.035228	H1A	0.441598	0.152374
C7	−0.100223	0.047529	H3	0.120453	−0.021902
C8	−0.105182	0.066550	H4	0.115718	−0.039233
C9	−0.170779	−0.039694	H6	0.107193	−0.044407
C10	0.071590	0.054893	H7	0.111141	−0.032910
C11	−0.025722	−0.053511	H8	0.110947	−0.032869
C12	0.134914	0.175776	H9	0.100320	−0.048448
N13A	−0.667324	−0.301155	H12	0.142282	0.000809
C14A	0.307431	0.090907	H19A	0.118673	−0.029954
C19A	−0.116622	0.040992	H18A	0.133527	−0.025674
C18A	−0.117644	0.116177	H16A	0.129260	−0.025568
C17A	−0.113146	−0.195187	H15A	0.115315	−0.021144
C16A	−0.129133	0.117918	H25	0.121594	−0.029958
C15A	−0.115490	0.029124	H24	0.111203	−0.039773
S1	0.139726	0.048449	H22	0.133248	−0.027203
C20	−0.065008	−0.130366	H21	0.126348	−0.020243
C25	−0.142039	0.092173	H27A	0.186667	0.029537
C24	−0.144597	0.008330	H27B	0.180083	0.044702
C23	0.067436	−0.026114	H27C	0.178595	0.045170
(II)					
Molecule A					
S1	0.147175	0.042339	C20	−0.129885	0.093531
O1	−0.544534	−0.285662	C21	0.349118	0.015631
O2	−0.456455	−0.217528	C22	−0.511599	0.015631
N1	−0.495723	−0.196009	H1	0.105001	−0.029694
C1	0.083921	0.142987	H3	0.122224	−0.033847
C2	0.116389	−0.040314	H4	0.113196	−0.027098
C3	−0.111832	0.065448	H6	0.102320	−0.029148
C4	−0.132655	0.050532	H7	0.100734	−0.042637
C5	0.375924	0.129593	H8A	0.182445	0.035861
C6	−0.169037	−0.002515	H8B	0.170786	0.035489
C7	−0.161134	0.034273	H8C	0.160652	0.042268
C8	−0.208521	0.112817	H10	0.110833	−0.022375
C9	0.277180	0.048821	H11	0.118449	−0.023555
C10	−0.108030	0.026423	H13	0.121514	−0.029920
C11	−0.127835	0.109723	H14	0.112235	−0.035415
C12	−0.109963	−0.192375	H16	0.116275	−0.022827
C13	−0.107287	0.112575	H17	0.119981	−0.030955
C14	−0.097946	0.050628	H19	0.113697	−0.029077
C15	−0.078271	−0.136877	H20	0.123389	−0.030222
C16	−0.124712	0.089838	H22A	0.183094	0.021716
C17	−0.115997	0.063829	H22B	0.183992	0.036689
C18	0.079390	−0.035878	H22C	0.176370	0.067928
C19	−0.158743	0.015529			
Molecule B					
S2	0.138550	0.049538	C42	−0.100994	0.090692
O3	−0.543399	−0.286723	C43	0.367830	0.026859
O4	−0.461546	−0.225440	C44	−0.511983	0.023229
N2	−0.478529	−0.193035	H23	0.107593	−0.032370
C23	0.052061	0.137227	H25	0.108152	−0.029867
C24	0.131231	−0.044734	H26	0.108093	−0.023618
C25	−0.135155	0.063446	H28	0.104452	−0.029503
C26	−0.155473	0.010144	H29	0.093432	−0.043107
C27	0.367903	0.133177	H30A	0.170222	0.036093
C28	−0.136440	0.039872	H30B	0.178998	0.037228
C29	−0.151017	0.034940	H30C	0.155501	0.045605
C30	−0.208873	0.112276	H32	0.104084	−0.022531
C31	0.250897	0.046280	H33	0.124636	−0.018370
C32	−0.098411	0.046193	H35	0.112416	−0.029597
C33	−0.140287	0.111205	H36	0.102806	−0.026716
C34	−0.078352	−0.197614	H38	0.123538	−0.024301
C35	−0.138524	0.110785	H39	0.105158	−0.039452
C36	−0.111190	0.035796	H41	0.126587	−0.027769
C37	−0.097438	−0.136377	H42	0.125997	−0.026483
C38	−0.099051	0.093825	H44A	0.185863	0.038680
C39	−0.139718	0.005169	H44B	0.181345	0.042069
C40	0.074910	−0.009922	H44C	0.186722	0.061414
C41	−0.118720	0.072705			

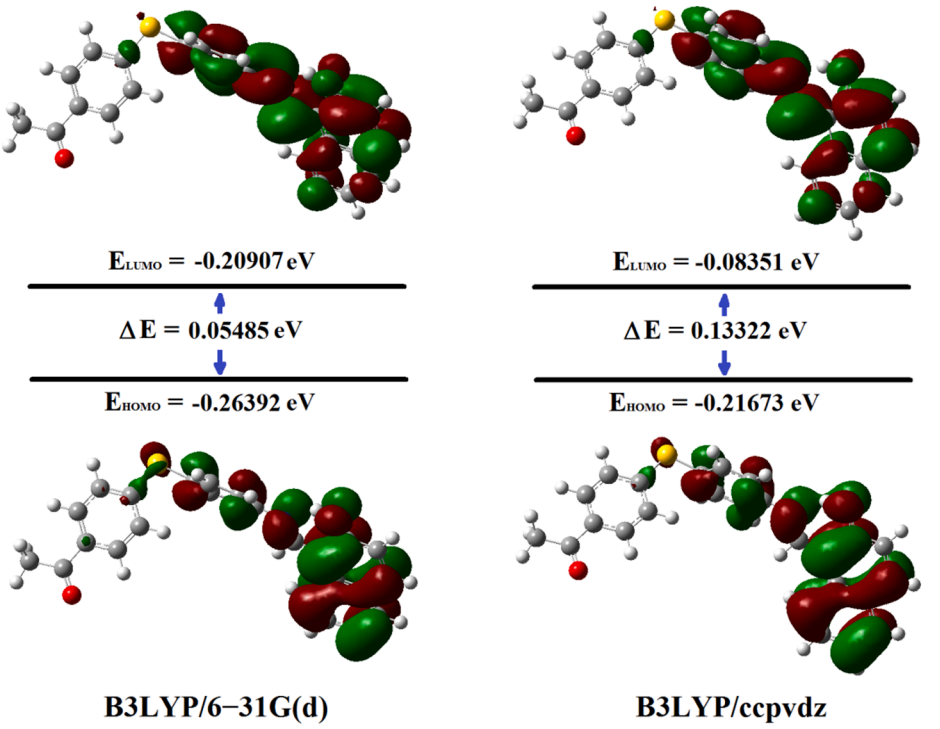

(a)

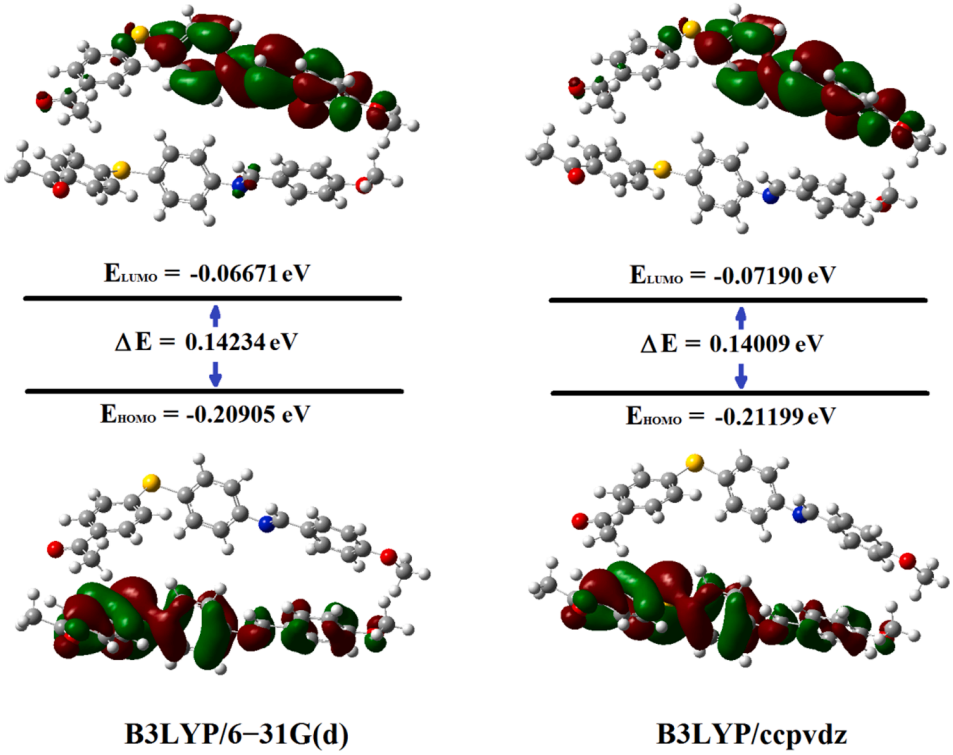

(b)

Fig. 4. Frontier orbitals for **(a)** compound (**I**) and **(b)** compound (**II**).

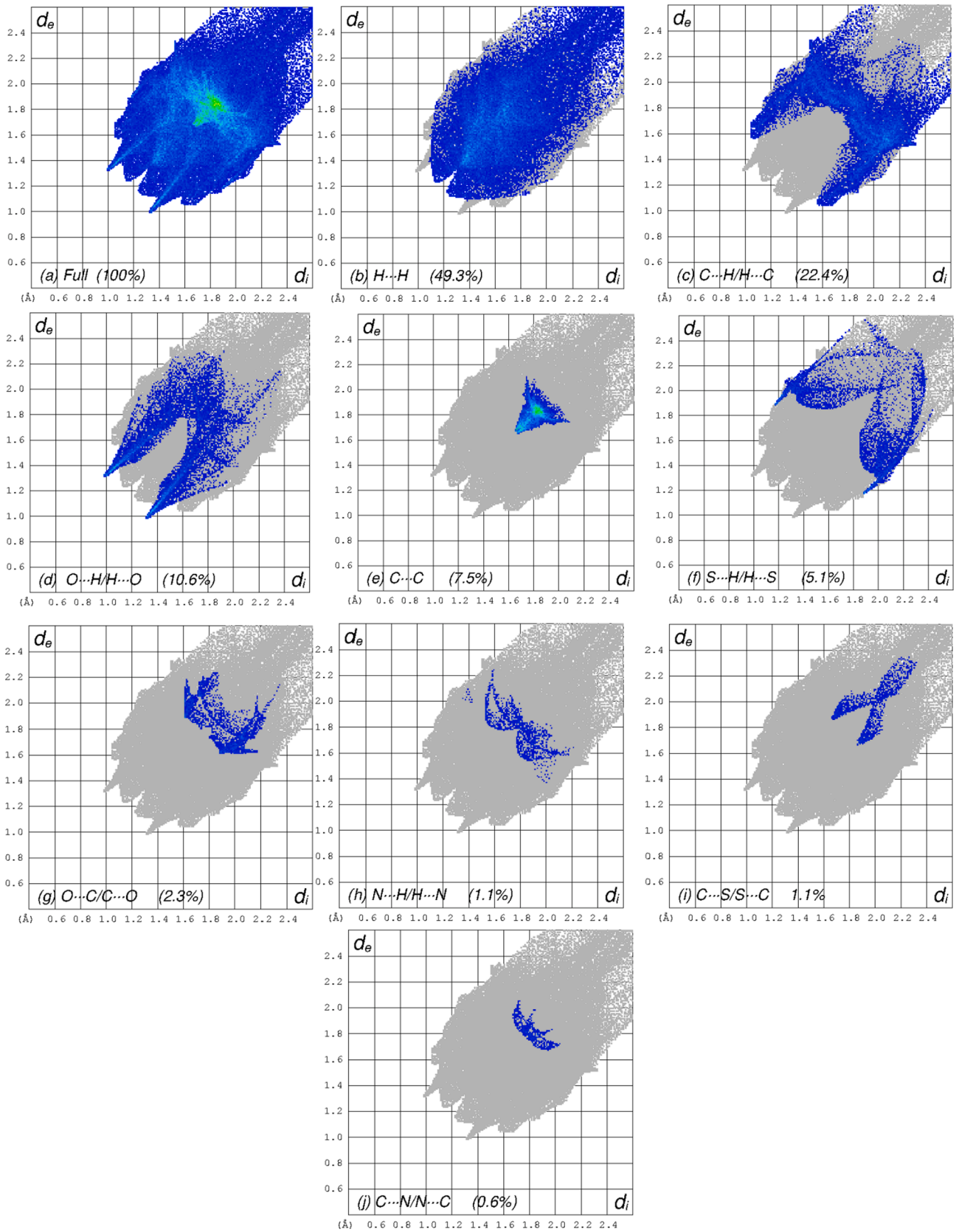

Fig. 5. 2D **FPs** of compound (I) showing full and decomposed intermolecular contacts.

3.3. Vibrational band assignments

The theoretical IR spectra of both compounds were predicted by both theory levels and selected wavenumbers were theoretically assigned to their corresponding vibration modes (Table 3). Thus, the asymmetric C—H stretching vibrations occur in the region [2911.55, 3090.41] cm^{-1} for (**I**) and in [2899.70, 3084.09] cm^{-1} for (**II**), obtained with the ***B3LYP/6-31G(d)*** method. On the other hand, the related values calculated with the ***B3LYP/cc-pvdz*** method were found to be respectively in the regions [3005.10, 3112.38] cm^{-1} and region [2923.62, 3127.41] cm^{-1}.

Furthermore, the asymmetric O—H stretching vibrations in (**I**) were observed at 2911.55 cm^{-1} (***B3LYP/6-31G(d)***) and 2835.07 cm^{-1} (***B3LYP/cc-pvdz***), and share additionally the respective wavenumbers 2992.62 cm^{-1} and 3005.10 cm^{-1} with the ν_{asym}(C—H) vibrations. Concerning the C═O stretching, they appear at 1701.94 cm^{-1} (***B3LYP/6-31G(d)***) and 1710.14 cm^{-1} (***B3LYP/cc-pvdz***) for (**I**). Similarly for compound (**II**), these vibration modes were observed within the range 1685.19–1697.69 cm^{-1} calculated by ***B3LYP/6-31G(d)*** and 1691.17–1704.48 cm^{-1} using the ***B3LYP/cc-pvdz*** level. Whereas, the asymmetric ν(C═N) of (**I**) are computed at 1613.17–1603.38 cm^{-1} (***B3LYP/6-31G(d)***) and 1611.79–1624.45 cm^{-1} (***B3LYP/cc-pvdz***), while those within (**II**) are predicted respectively in the range 1598.21–1602.26 cm^{-1} and 1642.76–1644.33 cm^{-1}.

3.4. Mulliken atomic charges

The computed *Mulliken* atomic charges of the two molecules are given in Table 4. It can be seen for ***B3LYP/6-31G(d)***, that only eight atoms in compound (**I**) show positive atomic charges with C26 having the highest value (0.358 a.u), whereas, all the remaining non-hydrogen atoms display negative ones with a highest value observed for N13A (−0.667 a.u). Additionally, the hydrogens' charges are in the range [0.100 a.u, 0.442 a.u] with the highest value attributed to H1A. Similarly, the ***B3LYP/cc-pvdz*** method gave rise respectively to highest negative and positive atomic charge magnitudes of −0.301 a.u and 0.118 a.u computed for N13A and C16A. Additionally, only eleven negative atomic charges were observed for the non-hydrogen atoms, while the hydrogen atoms showed values that vary from −0.048 a.u to 0.152 a.u related to H1A.

On the other hand, the values obtained for compound (**II**) using the basis ***B3LYP/6-31G(d)*** show that molecule **A**'s atoms (S1, C1, C2, C5, C9, C18, C21) and molecule **B**'s atoms (S2, C23, C24, C27, C31, C40, C43) display positive atomic charges. Moreover, the highest positive and negative values were respectively observed for C5 (0.376 a.u), O1 (−0.544 a.u) in **A** and C27 (0.368 a.u), O3 (−0.543 a.u) in **B**. Concerning the hydrogen atoms, their values are varying in the range [0.101 a.u, 0.184 a.u] for **A** and [0.093 a.u, 0.187 a.u] for **B**, with highest magnitudes computed respectively for H22B and H44C. However at the ***B3LYP/cc-pvdz*** level, the negative atomic charges we observed for (O1, O2, N1, C2, C6, C12, C15, C18,) in **A** and for (O3, O4, N2, C24, C34, C37, C40) of **B**, which display high values for O1 (−0.286 a.u) and O3 (−0.287 a.u), respectively. The highest positive ones were found to be 0.143 a.u and 0.137 a.u, which were obtained correspondingly for C1 (**A**) and C23 (**B**). Furthermore, the charge of the hydrogens H22C (**A**) and H44C (**B**) have the maximum magnitudes of 0.068 a.u and 0.061 a.u among the remaining hydrogen atoms.

3.5. Frontier molecular orbitals analysis

The most important molecular orbitals are the highest occupied (HOMO) and the lowest unoccupied molecular orbitals (LUMO) called the frontier molecular orbitals (FMOs). The HOMO–LUMO gap is considered significant when it relates to specific electrons' movements and may be most important for single electron transfer. This is useful for a number of reactions and has huge implications in organic semiconductors; the field where this gap is the most important. It has been found that molecules with large HOMO–LUMO gap are generally stable and unreactive, as well as the conductivity was shown to have an exponential relation with band gap energy [62–64]. Furthermore, the more negative LUMO energy values are the more chemically active the molecules will be [62,64], with the LUMO values being hence considered as activity descriptors. It was also reported that the molecular sites where the LUMO orbitals are distributed play an important role in the biological activities of compounds [65].

Thus, HOMO-LUMO distributions over the surface of a given molecular structure provide useful information for the identification of molecular activity. Accordingly, the FMOs were anticipated for both compounds by means of the ***B3LYP/6-31G(d)*** and ***B3LYP/cc-pvdz*** methods and are depicted in Fig. 4. HOMO orbitals are actually located over the oxo-naphthalene fragment for compound (**I**) and over the sulfanylphenylethanone moiety for compound (**II**), whereas, the LUMO orbitals are situated on compound (**I**)'s aminophenyl moiety and on compound (**II**)'s methoxybenzylidene-aminophenyl fragment.

According to the more refined basis set ***cc-pvdz***, the energy gaps between the HOMO and LUMO orbitals were found to be 0.133 eV for compound (**I**) and 0.140 eV for compound (**II**). As smaller values of band gap energy for a specific temperature lead to higher conductivity, it is observed that compound (**I**) is more conductive than compound (**II**). Moreover, (**I**) has lower LUMO energy than compound (**II**), being −0.084 eV *vs.* −0.072 eV. Consequently, one can conclude the higher activity of compound (**I**).

3.6. Hirshfeld surface (HS) analysis

The **HS** is a region of the crystal space around the molecule that can be considered as the frontier between regions where the electron distribution is dominated by the contribution of the reference molecule (interior) and of the neighboring molecules in the crystal (exterior). The **HS**s of both compounds' asymmetric units were mapped using the normalized contact distances (d_{norm}) which encompass two parameters, namely: d_e representing the distance of any surface point nearest to the internal atom and d_i which represent the distance of the surface point nearest to the exterior atom and also with the *van der Waals* radii of the atoms (r^{vdw}). The function d_{norm} is positive or negative where the contacts are greater or shorter than the *vdW* radii respectively, and is given with the following formula:

$$d_{norm} = \frac{\left(d_i - r_i^{vdW}\right)}{r_i^{vdW}} + \frac{\left(d_e - r_e^{vdW}\right)}{r_e^{vdW}}$$

Thus, the resulting **HS** displays red-white-blue colored scheme, where red displays shorter interactions, white is employed for contacts around the *vdW* radii separation and blue shows longer contacts. Additionally, to get more information about the weak contacts in both crystal packing, we have mapped the related **HS** over the *shape index* function. In this purpose, the minimum and maximum values of a particular function assume respectively the colors red (concave) and blue (convex), while intermediate values range from yellow to green [66]. Consequently, the *shape index* property (S) is defined by the following function:

$$S = \frac{2}{\pi}\arctan\left(\frac{\kappa_1 + \kappa_2}{\kappa_1 - \kappa_2}\right)$$

where κ_1 and κ_2 are the curvatures of the **HS** at the point under analysis, while S is a dimensionless measure of local shape at the surface. Accordingly, the resulting *shape index* is adopted as a tool allowing to visualize the π···π stacking by the presence of adjacent red and blue triangles.

On the other hand, we have decomposed the overall fingerprint plots **FP**s (Fig. 5.a and Fig. 6.a) to highlight particular important contacts in both compounds, which enabled the separation of the different

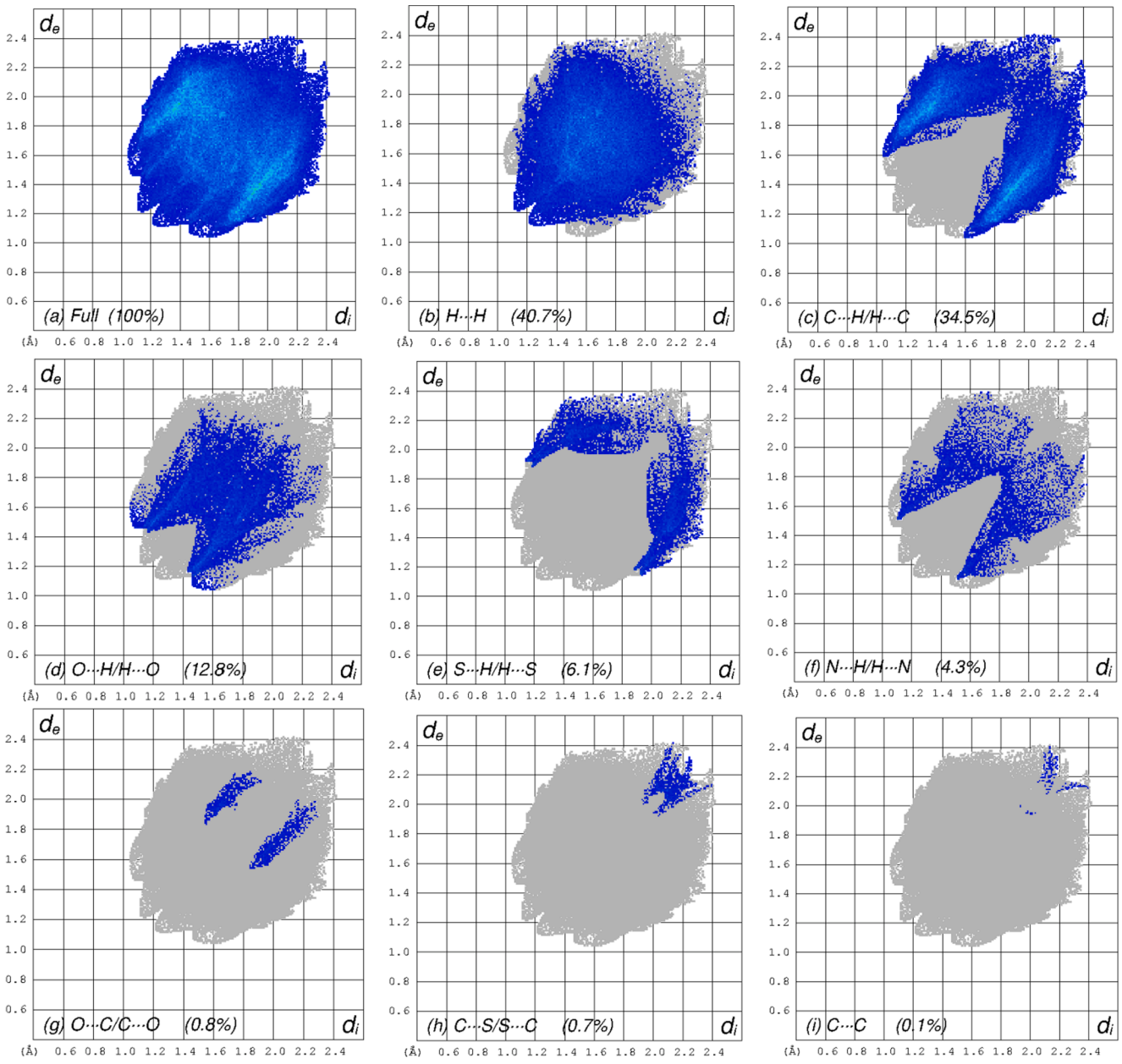

Fig. 6. 2D **FPs** illustrating the contacts in compound (**II**).

contributions from the contacts types commonly overlapping in the full **FP**. The **FPs** analysis of the crystal structures of (**I**) and (**II**) revealed that the contributions of the H···H intermolecular contacts are respectively 49.3 % (Fig. 5.b) and 40.7 % (Fig. 6.b). In order to emphasize these contacts and point out their leading interactions, we have mapped the **HS** of both compounds on the d_e representation, which showed mainly the existence of C—H…H—C interactions in both (**I**) and (**II**). The subsequent shortest contacts are thus attributed to the C21—H21…H15B—C15B (Fig. 7.c and 7.d) and C4—H4…H8B—C8 (Fig. 8.c) interactions with the respective bond lengths of about $d_i + d_e \sim 2.36$ Å in (**I**) and $d_i + d_e \sim 2.32$ Å in (**II**).

In the same manner, the second largest contacts in both compounds are the C···H/H···C ones, which appear as symmetric pair of wings and show a 22.4 % contribution (Fig. 5.c) to the total **HS** of compound (**I**) and 34.5 % (Fig. 6.c) in compound (**II**). Therefore, the prominent resulting interactions are mainly the C—H…π ones with a shortest value of $d_i + d_e \sim 2.60$ Å belonging to the C18A—H18A…C24 interaction (Fig. 7.b and 7.d) in (**I**) and ~ 2.64 Å related to the C29—H129…C6 interaction (Fig. 8.a) in (**II**). Thus, in both figures the presence of bright red concave-shaped sites on the surfaces of (**I**) and (**II**) mapped using the *shape index* property indicates the existence of the C—H···π interactions.

In both (**I**) and (**II**), the O···H/H···O contacts are the third most frequent ones and contribute respectively with 10.6 % (Fig. 5.d) and 12.8 % (Fig. 6.d) to the total *Hirshfeld* areas. These contacts appear also as two lateral spikes in the 2D **FP** maps with prominent short contacts at about $d_i + d_e = 2.3$ Å in the crystal structure of (**I**) and at $d_i + d_e = 2.49$ Å in (**II**), which correspond respectively to the C22—H22···O1A (Fig. 7.a) and C29—H29···O1 hydrogen bonds (Fig. 8.a), illustrated by representing the d_{norm} property which showed several red spots with different brightness.

As for the C···C contacts, they represent the π···π interactions which contribute significantly to the total **HS** of (**I**) comprising 7.5 % (Fig. 5.e), however they are negligible in (**II**) with only 0.1 % contribution (Fig. 6.i). The shortest interactions appear respectively at around $(d_i + d_e) \sim 3.32$ Å and ~ 4.18 Å, resulting from C6…C10 (Fig. 7.e and 7.f) and C39…C15 (Fig. 8.e), which were emphasized by building the surfaces of

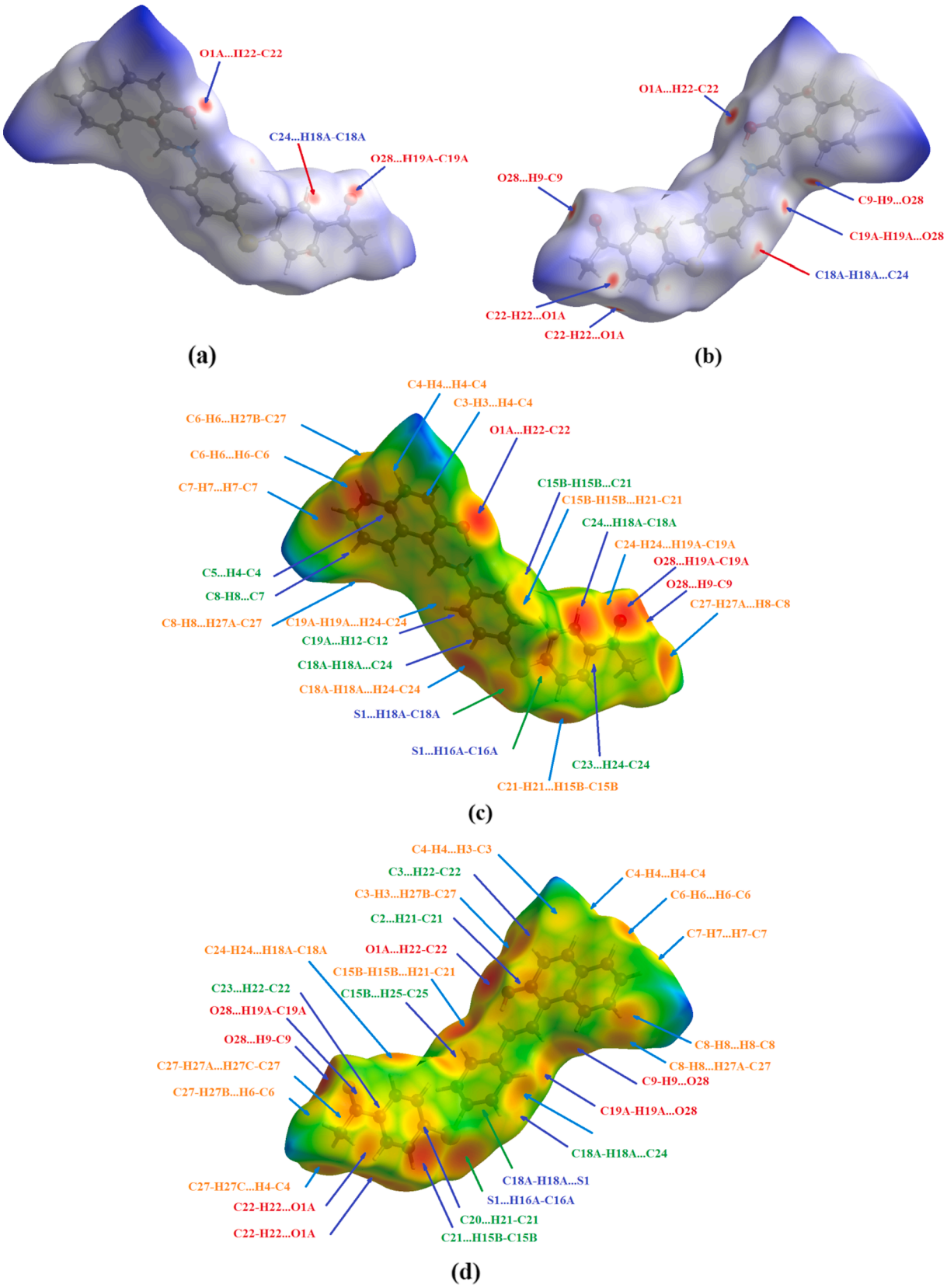

Fig. 7. Front and back views of the **HS**s displayed using the transparent mode for compound (**I**), mapped over **(a)**, **(b)** d_{norm}, **(c)**, **(d)** d_e and **(e)**, **(f)** *shape index* properties.

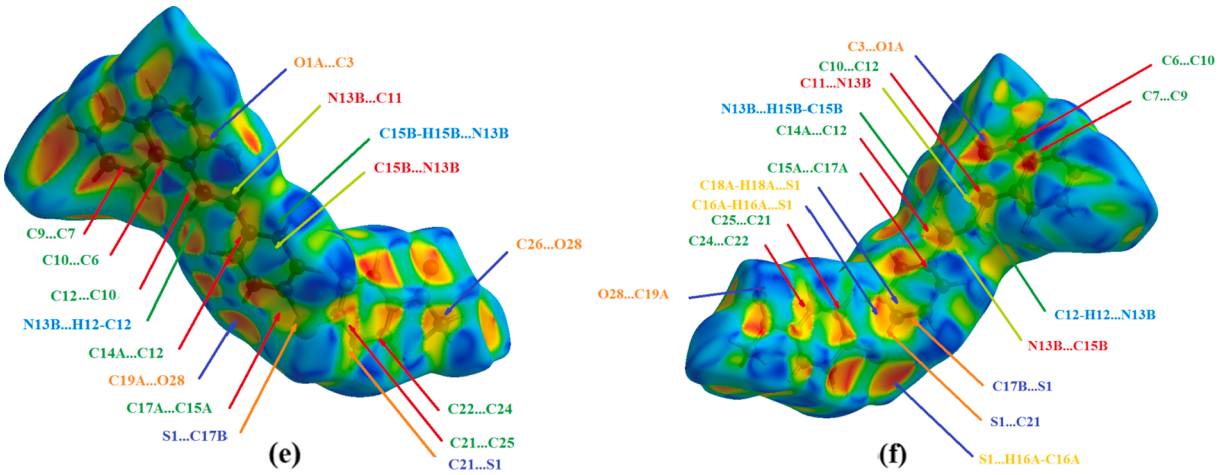

Fig. 7. (*continued*).

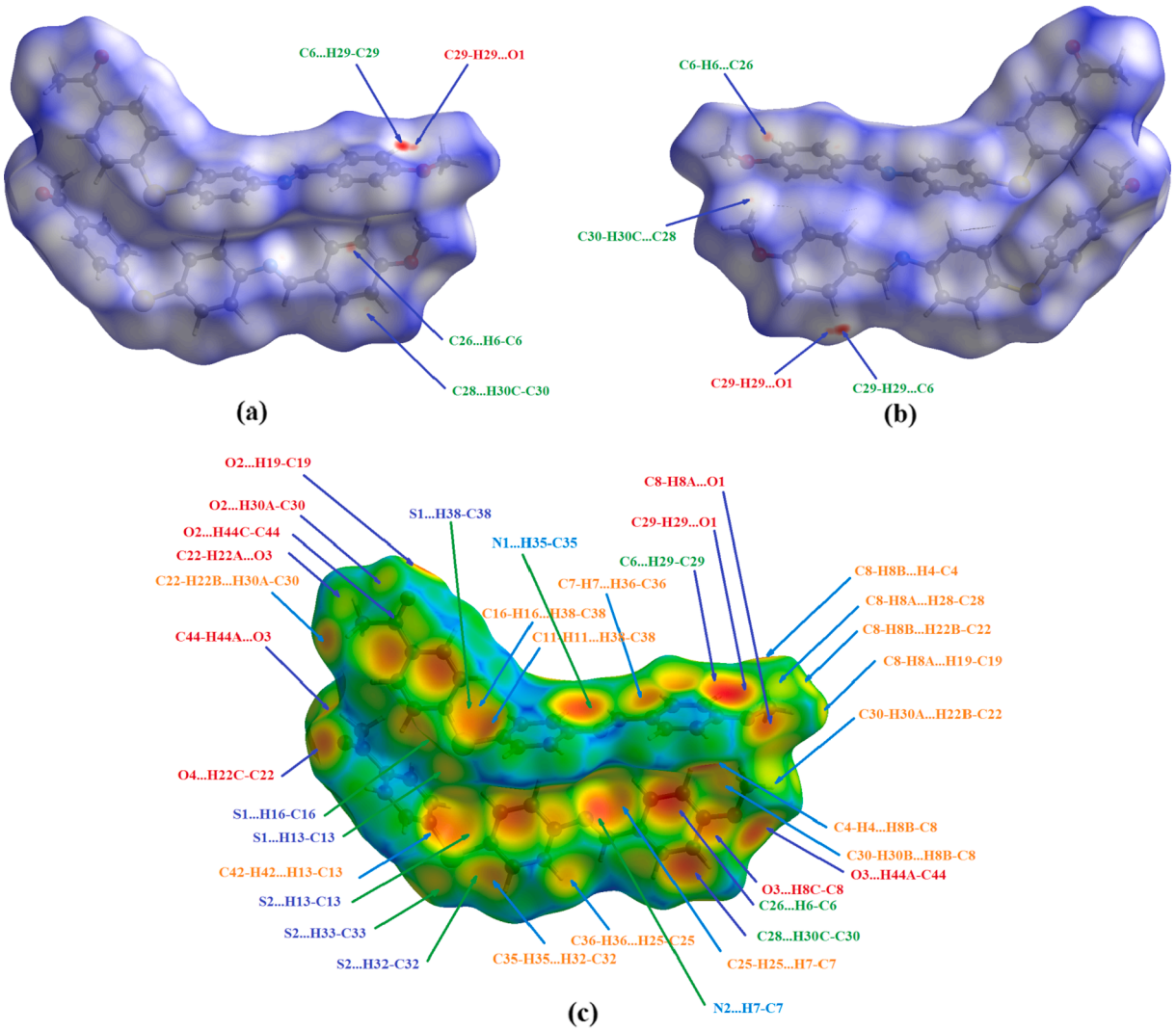

Fig. 8. Front and back views of the **HS**s of compound (**II**) mapped over **(a)**, **(b)** d_{norm}, **(c)**, **(d)** d_e and **(e)** *shape index* functions, showing the possible interactions.

both compounds taking into account the *shape index* function showing the most prominent intermolecular contacts. It is consequently evident that the molecules of (**I**) are connected to one another by stacking interactions, as it can appear from the inspection of the red and blue triangles on the *shape index* function. Indeed, these are characteristic π···π stacking arrangement of aromatic compounds in which the red

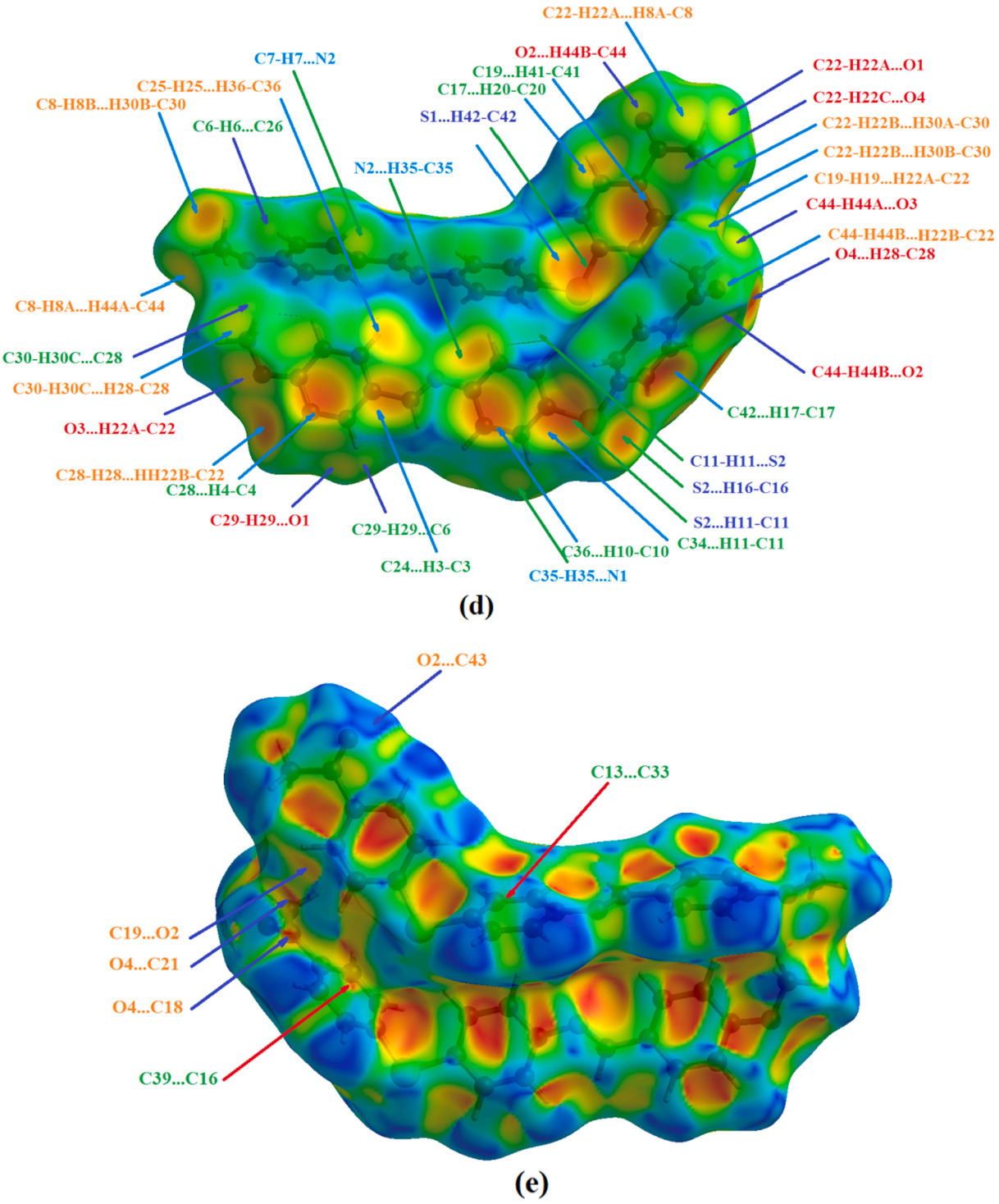

Fig. 8. (*continued*).

triangles are concave regions associated with atoms of the π···π stacked rings above them, while the blue triangles are convex regions indicating the aromatic ring atoms of the molecule inside the surface. On the contrary, it is clear that the crystal structure of compound (**II**) does not exhibit any important π···π stacking interactions since there is no evidence of the adjacent red and blue triangles on the *shape index* surface (Fig. 8.e).

In contrary, the N···H/H···N contacts show a minimal contribution in (**I**), 1.1 % (Fig. 5.h), and a notable one in (**II**), 4.3 % (Fig. 6.f). The shortest N···H/H···N contacts in (**I**) are located at $d_i + d_e = 3.38$ Å and at $d_i + d_e = 2.62$ Å in (**II**), and are related to the respective interactions C15B-H15B…N13B (Fig. 7.e and 7.f) and C7-H7…N2 (Fig. 8.c).

It is worthy to note that the S···H/H···S contacts present similar contributions of 5.1 % (Fig. 5.f) and 6.1 % (Fig. 6.e) in (**I**) and (**II**) respectively. These contacts show shortest distances of $d_i + d_e = 3.06$ Å in (**I**) and $d_i + d_e = 3.08$ Å in (**II**), which are attributed to the respective C16A-H16A…S1 (Fig. 7.f) and C38-H38…S1 (Fig. 8.c) interactions.

Moreover, weak O···C/C···O, C···S/S···C and C···N/N···C contacts were also observed and result from the π···*lp* interactions (Fig. 7.e, 7.f, 8. e and 8.f). However, they exhibit minimal contributions of respectively

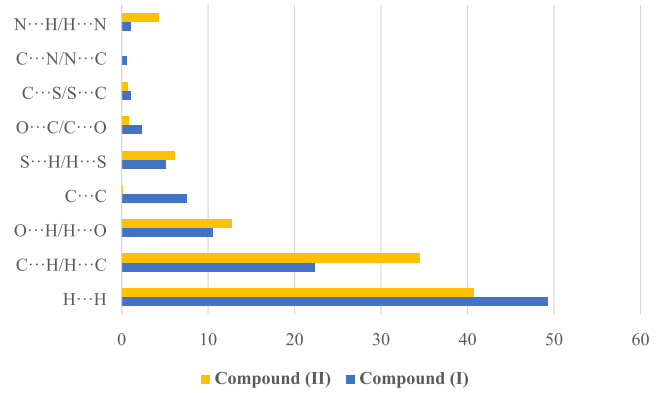

Fig. 9. Comparative contribution percentages of the different contacts in the studied structures.

2.3 % (Fig. 5.g), 1.1 % (Fig. 5.i), 0.6 % (Fig. 5.j) in (**I**), and 0.8 % (Fig. 6.g), 0.7 % (Fig. 6.h), 0.0 % in (**II**), reflecting negligible effect on the molecular packing. It is therefore clear that the C—H···H—C, C—H···π and C—H···O interactions, were the most significant contributors among the interacting atoms. This finding therefore mentions the importance of these contacts in the cohesion of the crystal structures packing. The histogram given in Fig. 9 illustrates the importance of these contacts by providing comparatively their percentages in the compounds (**I**) and (**II**).

3.7. Molecular docking

We have considered the approximate free binding energy used in AutoDock4 as a scoring function by assuming that it represents a linear combination of the pairwise terms: $\Delta G = \Delta G_{vdW} + \Delta G_{Hbond} + \Delta G_{elec} + \Delta G_{conform} + \Delta G_{tor} + \Delta G_{desolv}$. The molecular mechanics terms ΔG_{vdW}, ΔG_{Hbond}, ΔG_{elec} and $\Delta G_{conform}$ are respectively the dispersion/repulsion, hydrogen bonding, electrostatic energies and deviations from the covalent geometry. Whereas, ΔG_{tor} models the restriction of internal rotors, global rotation and translation. The ΔG_{desolv} term represents the desolvation and the hydrophobic effect. The ten (10) binding poses of ligands (**I**) and (**II**) to the actives sites of **1JIJ** and **2XCT**, obtained after docking are ranked in Table 5 from the lowest to the highest energetic conformation mode.

The results (Table 5) show the best docking scores for compounds (**I**) and (**II**), whereas the most energetically favorable conformation was considered in both cases and the related decomposed energies are illustrated in Table 6. Therefore, the free binding energies of (**I**) and (**II**) against **1JIJ** are respectively −9.91 kcal/mol and −8.22 kcal/mol, with an estimated inhibition constant K_i of 54.29 nM and 944.09 nM, respectively. Additionally, the free binding energies of the studied ligands against the PDB entry **2XCT** were found to be nearly equal, being respectively −7.17 kcal/mol and −7.64 kcal/mol, which relate correspondingly to the inhibitory activity factors of 5.54 mM and 2.52 *m*M.

Where: $\Delta G_{ntermol}$ is the final intermolecular energy ($\Delta G_{vdW} + \Delta G_{Hbond} + \Delta G_{desolv} + \Delta g_{elec}$), $\Delta G_{tot\ int}$ is the final total internal energy, ΔG_{tor} is the torsional free energy and $\Delta G_{unbound}$ is the unbound system's energy.

The default parameter for the hydrogen donor and acceptor distance D…A was set to 3.48 Å and the D—H…A angle was considered in the range 120°–180°. Therefore, the visualization of the binding pockets of both receptors with Chimera [59] showed the hydrogen bonds formed between the targets and the two ligands separately (Fig. 10). Consequently, as depicted in Table 7 that compound (**I**) interacts with **1JIJ** through three hydrogen bonds (Fig. 10.a), namely N—H…O one built with Val_{224} (hydrophobic) acting as a donor, S—H…O interaction formed with the S atom of Cys_{37} (polar) and O—H…O hydrogen-bonding linking the ligand hydrogen H1 and the Gly_{38} (nonpolar) receptor oxygen. Furthermore, an extra weak O—H…O interaction, shown in (Fig. 11.a) as green dashed line, was observed between (**I**) and Val_{191} (hydrophobic) as an H-bond acceptor. As for compound (**II**), it showed an N—H…O interaction (Fig. 10.b) built up with the aminoacid residue Ser_{194} (polar).

As for the **2XCT** receptor, it interacts with both ligands by forming two hydrogen bonds with each one separately. Thus, ligand (**I**) displays an N—H…O and an O—H…O interactions (Fig. 10.c) built respectively with the residues Arg_{1122D} (positively charged) and Ser_{1084B} (polar). Similarly, (**II**) shows two hydrogen bonds namely N—H…S and N—H…O (Fig. 10.d) formed respectively with the aminoacids Asn_{1153B} (polar) and His_{1081B} (aromatic).

Moreover, the hydrophobic contacts could be considered when a ligand's carbon or halogen atom comes within 4.0 Å from a receptor's carbon or sulfur [67]. Consequently, both ligands interact with the two receptors by means of hydrophobic contacts analyzed using Ligplot [68] and depicted in (Fig. 11) as red arcs with spokes radiating towards the ligand atoms they contact where the contacted atoms are drawn with spokes radiating back. As a result, both ligands interact with the **1JIJ** receptor by sharing the hydrophobic contacts built through the residues Gln_{174}, Asp_{177}, Asp_{40}, Tyr_{170}, Gly_{193}, Pro_{222}, Leu_{223}, Gln_{196} and Thr_{75} (Fig. 11.a & 11.b). It is worth to be noted that Asp_{40}, Gly_{193}, Asp_{177}, Gln_{196} and Tyr_{170} belong to the active sites observed in the crystal structure of the complex **1JIJ**-SB-239629 [57].

Table 5
Binding affinities ΔG (kcal/mol) of (**I**) and (**II**)'s conformations to the active sites of **1JIJ** and **2XCT**.

	1st	2nd	3rd	4th	5th	6th	7th	8th	9th	10th
Ligand/Receptor	**1JIJ**									
(I)	−9.91	−9.88	−9.75	−9.68	−9.53	−9.37	−9.36	−9.23	−8.90	−8.72
(II)	−8.22	−8.17	−7.95	−7.94	−7.93	−7.81	−7.63	−7.62	−7.59	−7.54
	2XCT									
(I)	−7.17	−6.96	−6.93	−6.84	−6.82	−6.74	−6.29	−6.16	−5.75	−5.75
(II)	−7.64	−7.56	−7.49	−6.65	−6.52	−6.50	−6.36	−6.23	−6.20	−6.20

Table 6
Component terms of the lowest free binding energies (kcal/mol) of the two ligands with the active sites of **1JIJ** and **2XCT**.

	$\Delta G_{vdW} + \Delta G_{Hbond} + \Delta G_{desolv}$	ΔG_{elec}	$\Delta G_{intermol}$	$\Delta G_{tot\ int}$	ΔG_{tor}	$\Delta G_{unbound}$
Ligand/Receptor	**1JIJ**					
(I)	−11.59	−0.11	−11 0.70	−1.19	+1.79	−1.19
(II)	−9.89	−0.12	−10.01	−0.65	+1.79	−0.65
	2XCT					
(I)	−8.88	−0.08	−8.96	−1.38	+1.79	−1.38
(II)	−9.27	−0.16	−9.43	−0.88	+1.79	−0.88

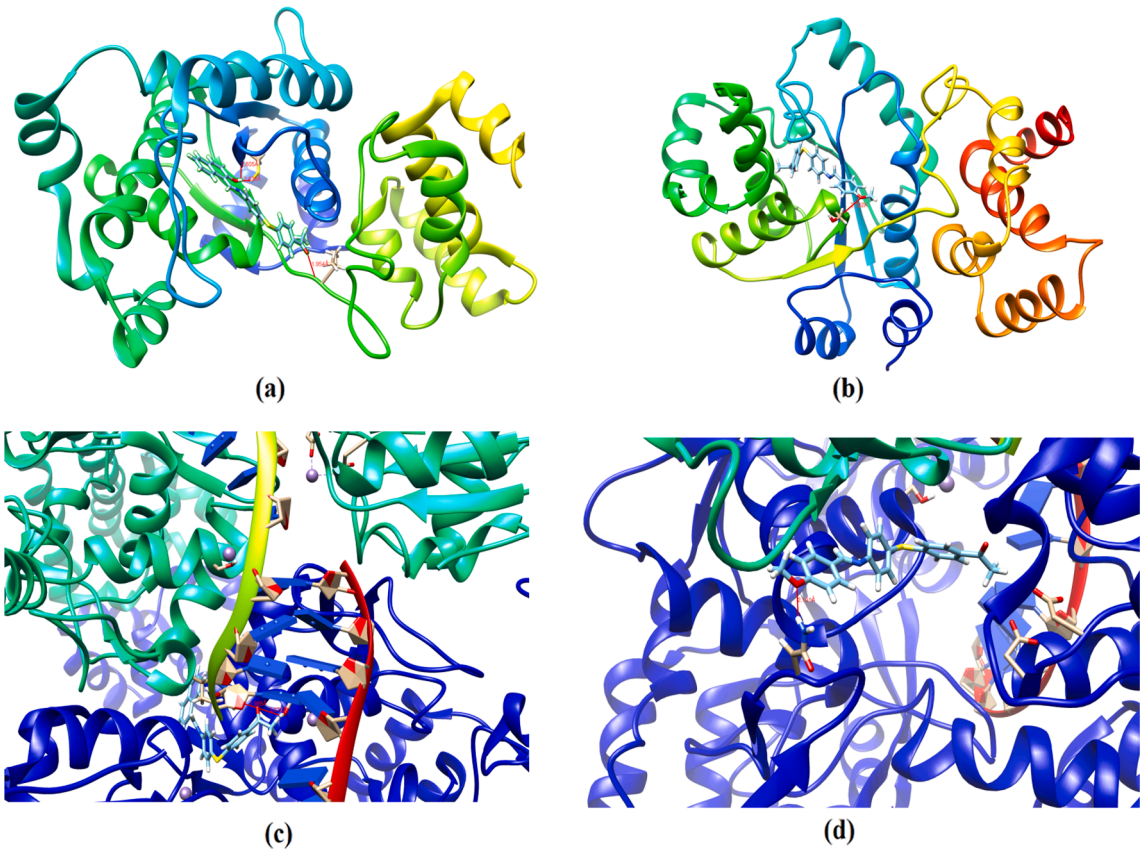

Fig. 10. Docking poses showing (**I**) interacting with residues in the binding sites of the targets (a) **1JIJ** and (c) **2XCT**. Predicted binding modes of (**II**) at the binding pockets of (b) **1JIJ** and (d) **2XCT**.

Table 7
Geometric parameters of the hydrogen bonds formed in the binding pockets between the receptors **1JIJ**, **2XCT** and the ligands (**I**), (**II**).

	Aminoacid residue	D—H…A	D…A (Å)	H…A (Å)
Ligand/Receptor	**1JIJ**			
(I)	Gly_{38}	O…H—O	3.431	2.805
	Val_{224}	N—H…O	2.962	1.954
	Cys_{37}	S—H…O	3.156	2.436
	Val_{191}	O…H—O	3.47	
(II)	Ser_{194}	N—H…O	3.397	2.733
	2XCT			
(I)	Ser_{1084B}	O—H…O	3.884	3.072
	Arg_{1122D}	N—H…O	2.980	1.988
(II)	His_{1081B}	N—H…S	3.244	2.419
	Asn_{1153B}	N—H…O	3.009	2.101

Furthermore, ligand (**II**) shows π…π stacking [69,70] linking the ligand's sulfanyl-phenylethanone ring with the Tyr_{170} residue in **1JIJ** (Fig. 12.a). It presents additionally short C…N, S…O, O…O, C…O, N…N, C…C binding contacts ranging from 0.82 Å to 3.75 Å as shown in Fig. 11.b as purple lines. On the other hand, both the ligands (**I**) and (**II**) bind to the **2XCT** macromolecule *via* hydrophobic contacts. Hence, we have observed that **2XCT** forms hydrophobic contacts with (**I**) resulting from the aminoacid residues Arg_{1122D}, Ser_{1084B}, Asn_{1182B}, Gly_{1082B}, His_{1081B}, Phe_{1123D}, Pro_{1080B}, Tyr_{1150B}, Lys_{1066D}, Met_{1075B}, Gly_{1076B} and Ala_{1068D}, as well as the DNA base Dg_{9G} (Fig. 11.c and 11.d). While, this macromolecule is hydrophobically connected to (**II**) through Arg_{1122D}, Pro_{1080B}, Tyr_{1150B}, Tyr_{1064D}, Asn_{1153B}, Glu_{1125D}, Asp_{1151B}, Lys_{1066D}, Lys_{1065D}, Phe_{1123D}, Met_{1075B}, Asp_{508B}, Gly_{582B}, Gly_{1076B} and His_{1081B}. Additionally, ligand (**I**) connect to **2XCT** through a π -cation interaction of 4.54A involving the charged fragment of Arg_{1122D}. As for (**II**), it shows a 4.80A π…π stacking linking it with Phe_{1123D} (Fig. 12.b).

4. Conclusion

Two 4-amino-4′-acetyldiphenyl sulfide-based Schiff bases, namely 1-[4-({4-[(E)-(2-hydroxynaphthalen-1-yl)methylideneamino]phenyl}sulfanyl)phenyl] ethanone (**I**) and (E)-1-[4-({4-[(4-methoxybenzylidene) amino]phenyl}-sulfanyl)phenyl]ethan-1-one (**II**) were studied and their structural features discussed. The crystal structures of both compounds are known; they crystallize respectively in the monoclinic *Cc* and the triclinic *P*1 space groups. The asymmetric unit of (**I**) contains one molecule, whereas the asymmetric unit of (**II**) encloses two crystallographically independent molecules. The molecules were then optimized by the ***B3LYP*** functional in conjunction with the ***6-31G(d)*** and ***cc-pvdz*** basis sets. It was therefore found that both methods reproduce very well the geometry of the studied molecules and compare well with their experimental geometric parameters. Furthermore, the IR vibrational wavenumbers and the *Mulliken* atomic charges of both molecules were investigated. The evaluation of the HOMO orbitals showed that they are located over the *oxo*-naphthalene fragment for (**I**) and over the sulfanyl-phenylethanone moiety for (**II**). Whereas, the LUMO orbitals were found to be situated on the aminophenyl moiety in (**I**) and on the methoxybenzylidene-aminophenyl fragment in (**II**). Moreover, according to the orbital and band gap energies, it was found that (**I**) is more conductive and active than (**II**). The **HS** analysis and the subsequent 2D-**FP**s indicated that the leading contacts in both structures are H···H esulting mainly from the C—H…H—C interactions, followed by the C···H/H···C ones which emanated from the C—H···π interactions. Moreover, C—H···O, C—H···N, C—H···S and π···*lp* interactions were also observed in (**I**) and (**II**). However, compound (**I**) showed interesting π···π stacking. Additionaly, we performed an *in silico* study of both ligands by investigating their binding modes towards the macromolecules *S. aureus* tyrosyl-tRNA synthetase **1JIJ** and *S. aureus* topoisomerase II DNA gyrase

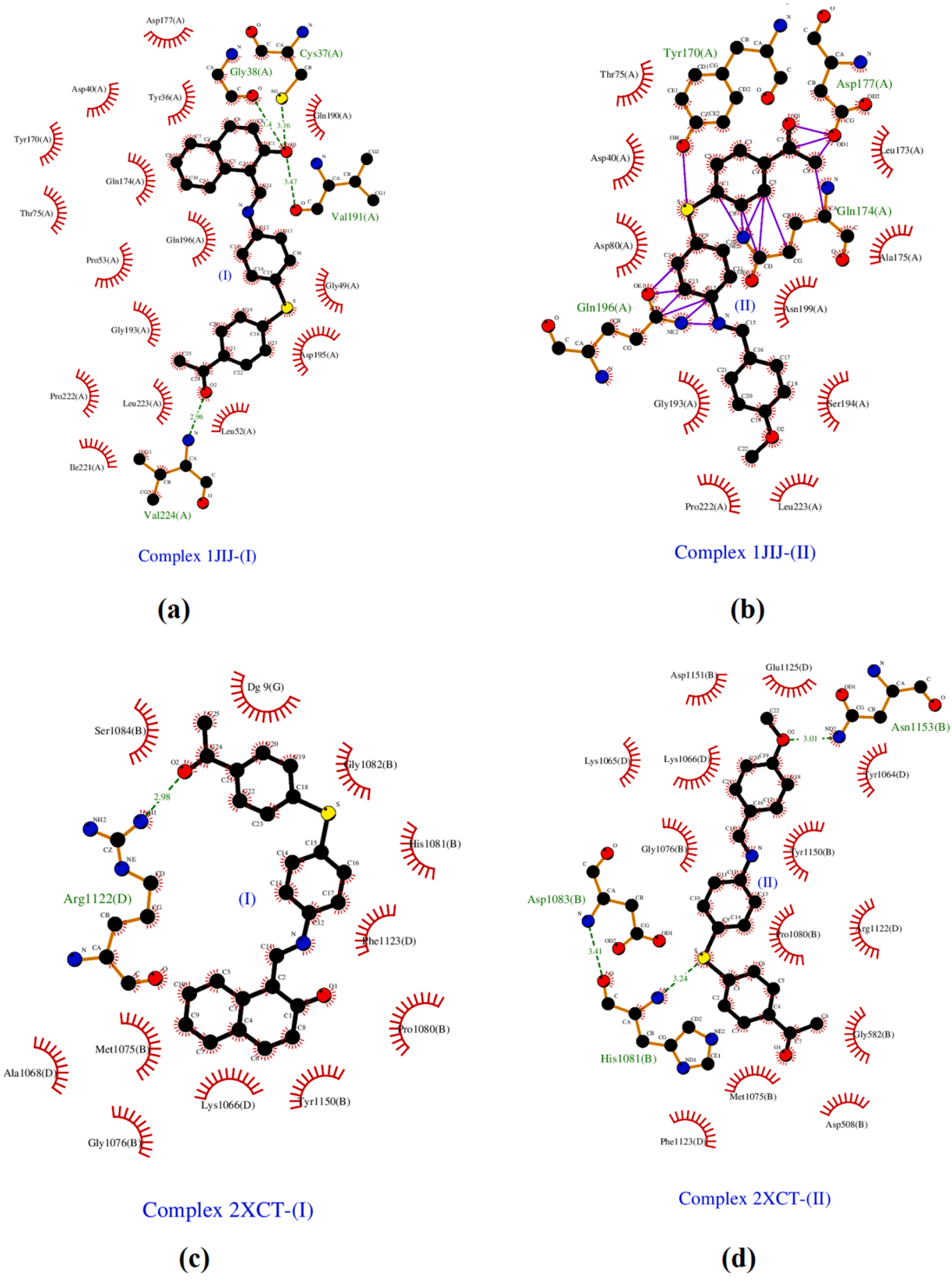

Fig. 11. Hydrophobic contacts and hydrogen bonding observed between the ligands and the targets. Hydrogen bonds are depicted as dashed lines and hydrophobic contacts as arcs.

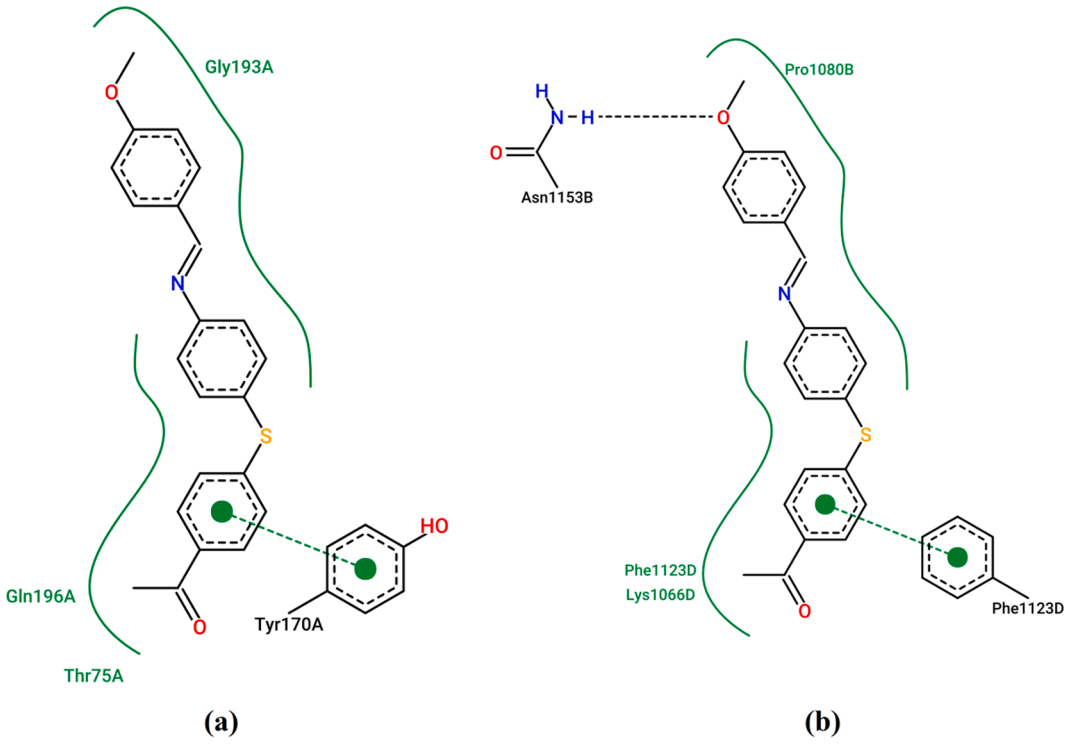

Fig. 12. $\pi\ldots\pi$ stacking built between the ligand (**II**) and (a) **1JIJ**, (b) **2XCT**.

2XCT using a molecular docking analysis. It was found that (**I**) and (**II**) bind to both the receptors and interact with their binding sites *via* hydrogen bonds, hydrophobic contacts, π-cation interactions and π…π stacking. As a result, the ligands (**I**) and (**II**) could consequently be considered as potential inhibitors of the MRSA enzymes **1JIJ** and **2XCT**.

CRediT authorship contribution statement

Soumia Kadri: Writing – original draft, Investigation, Conceptualization, Resources. **Amani Direm:** Writing – original draft, Visualization, Writing – review & editing, Validation, Resources, Conceptualization, Supervision. **Hamza Athmani:** Writing – original draft, Visualization, Validation. **Brahim El Bali:** Writing – original draft, Visualization, Validation. **Cemal Parlak:** Writing – original draft, Writing – review & editing, Validation, Resources. **Rabihe Hebbachi:** Investigation, Resources, Conceptualization.

Declaration of Competing Interest

The authors declare that they have no known competing financial interests or personal relationships that could have appeared to influence the work reported in this paper.

Acknowledgements

AD would like to acknowledge the fund of the Ministry of Higher Education and Scientific Research MESRS and Abbes Laghrour University of Khenchela (Algeria) under the project number: B00L01UN400120210002 (PRFU).

References

[1] E.Y. Furuya, F.D. Lowy, Antimicrobial-resistant bacteria in the community setting, Nat. Rev. Microbiol. 4 (1) (2006) 36–45.
[2] I.M. Gould, The clinical significance of methicillin-resistant Staphylococcus aureus, J. Hosp. Infect. (2005) 61277–61282.
[3] S.J. Schweon, MRSA extends its reach. RN 6933-34 (2006) 36.
[4] C. Kallberg, C. Ardal, B.H. Salvesen, E. Klein, E.M. Martinez, M. Lindbaek, K. Outterson, J.A. Rottingen, R. Laxminarayan, Introduction and geographic availability of new antibiotics approved between 1999 and 2014, PLoS ONE. 13 (2018) e0205166.
[5] N.G. Simoes, A.F. Bettencourt, N. Monge, I.A.C. Ribeiro, Novel Antibacterial Agents: An Emergent Need to Win the Battle Against Infections, Mini Rev. Med. Chem. 17 (2017) 1364–1376.
[6] E.Y. Garoy, Y.B. Gebreab, O.O. Achila, D.G. Tekeste, R. Kesete, R. Ghirmay, R. Kiflay, T. Tesfu, Methicillin-Resistant Staphylococcus aureus (MRSA): Prevalence and Antimicrobial Sensitivity Pattern among Patients-A Multicenter Study in Asmara, Eritrea, Can. J. Infect. Dis. Med. Microbiol. 2019 (2019) 8321834.
[7] The Center for Disease Dynamics, Economics & Policy (CDDEP), Inc. 2021. The state of the world's antibiotics in 2021. 2021. https://cddep.org/wp-content/uploads/2021/02/The-State-of-the-Worlds-Antibiotics-in-2021.pdf (accessed April 20, 2022).
[8] Global antimicrobial resistance and use surveillance system (GLASS) report. 2021. Geneva: World Health Organization. 2021. https://apps.who.int/iris/rest/bitstreams/1350455/retrieve (accessed April 20, 2022).
[9] E. Tacconelli, E. Carrara, A. Savoldi, S. Harbarth, M. Mendelson, D. L. Monnet, C. Pulcini, G. Kahlmeter, J. Kluytmans, Y. Carmeli, M. Ouellette, K. Outterson, J. Patel, M. Cavaleri, E. M. Cox, C. R. Houchens, M. L. Grayson, P. Hansen, N. Singh, U. Theuretzbacher, N. Magrini & the WHO Pathogens Priority List Working Group. Discovery, research, and development of new antibiotics: the WHO priority list of antibiotic-resistant bacteria and tuberculosis. Lancet Infect. Dis. 18, 318–327 (2018).
[10] R.J. Fair, Y. Tor, Antibiotics and Bacterial Resistance in the 21st Century, Perspect. Medicin. Chem. 6 (2014) PMC.S14459, https://doi.org/10.4137/PMC.S14459.
[11] L.L. Silver, Multi-targeting by monotherapeutic antibacterials, Nat. Rev. Drug Discov. 6 (1) (2007) 41–55.
[12] E. Oldfield, X. Feng, Resistance-Resistant Antibiotics, Trends Pharmacol. Sci. 35 (2014) 664–674.
[13] V.L. Simpkin, M.J. Renwick, R. Kelly, E. Mossialos, Incentivising innovation in antibiotic drug discovery and development: Progress, challenges and next steps, J. Antibiot. (Tokyo) 70 (2017) 1087–1096.
[14] A.R. Fersht, J.W. Knill-Jones, H. Bedouelle, G. Winter, Reconstruction by site-directed mutagenesis of the transition state for the activation of tyrosine by the tyrosyl-tRNA synthetase: A mobile loop envelopes the transition state in an induced-fit mechanism, Biochem. 27 (5) (1988) 1581–1587.
[15] Z.-P. Xiao, T.-W. Ma, M.-L. Liao, Y.-T. Feng, X.-C. Peng, J.-L. Li, Z.-P. Li, Y. Wu, Q. Luo, Y. Deng, X. Liang, H.-L. Zhu, Tyrosyl-tRNA synthetase inhibitors as antibacterial agents: Synthesis, molecular docking and structure–activity relationship analysis of 3-aryl-4-arylaminofuran-2(5H)-ones, Eur. J. Med. Chem. 46 (10) (2011) 4904–4914.
[16] P. Schimmel, J. Tao, J. Hill, Aminoacyl tRNA synthetases as targets for new anti-infectives, FASEB J. 12 (15) (1998) 1599–1609.

[17] M. Barančoková, D. Kikelj, J. Ilaš, Recent progress in the discovery and development of DNA gyrase B inhibitors, Future Med. Chem. 10 (10) (2018) 1207–1227, https://doi.org/10.4155/fmc-2017-0257.
[18] A.D. Bates, A. Maxwell, DNA Topology, Oxford University Press, Oxford, 2005.
[19] S.H. Chen, N.-L. Chan, T.-S. Hsieh, New mechanistic and functional insights into DNA topoisomerases, Annu. Rev. Biochem. 82 (1) (2013) 139–170, https://doi.org/10.1146/annurev-biochem-061809-100002.
[20] S.M. Vos, E.M. Tretter, B.H. Schmidt, J.M. Berger, All tangled up: how cells direct, manage and exploit topoisomerase function, Nat. Rev. Mol. Cell Biol. 12 (12) (2011) 827–841, https://doi.org/10.1038/nrm3228.
[21] N.G. Bush, K. Evans-Roberts, A. Maxwell, S.T. Lovett, DNA topoisomerases, EcoSal Plus 6 (2) (2015), https://doi.org/10.1128/ecosalplus.ESP-0010-2014.
[22] S.J. McKie, K.C. Neuman, A. Maxwell, DNA topoisomerases: advances in understanding of cellular roles and multi-protein complexes via structure–function analysis, BioEssays 43 (4) (2021) 2000286, https://doi.org/10.1002/bies.v43.410.1002/bies.202000286.
[23] F. Collin, S. Karkare, A. Maxwell, Exploiting bacterial DNA gyrase as a drug target: current state and perspectives, Appl. Microbiol. Biotechnol. 92 (3) (2011) 479–497, https://doi.org/10.1007/s00253-011-3557-z.
[24] E. Raczuk, B. Dmochowska, J. Samaszko-Fiertek, J. Madaj, Different Schiff Bases—Structure, Importance and Classification, Molecules. 27 (3) (2022) 787.
[25] L. Wang, W. Qin, X. Tang, W. Dou, W. Liu, Q. Teng, X. Yao, A selective, cell-permeable fluorescent probe for Al3+ in living cells, Org. Biomol. Chem. 8 (2010) 3751–3757.
[26] G. Saravanan, P. Pannerselvam, C.R. Prakash, Synthesis and anti-microbial screening of novel Schiff bases of 3-amino-2-methyl quinazolin 4-(3H)-one, J. Adv. Pharm. Technol. Res. 1 (2010) 320–325.
[27] D. Puthran, B. Poojary, N. Purushotham, N. Harikrishna, S.G. Nayak, V. Kamat, Synthesis of novel Schiff bases using 2-amino-5-(3-fluoro-4-methoxyphenyl)thiophene-3-carbonitrile and 1,3-disubstituted pyrazole-4-carboxaldehydes derivatives and their antimicrobial activity, Heliyon 5 (8) (2019) e02233, https://doi.org/10.1016/j.heliyon.2019.e02233.
[28] C.B. Sangani, J.A. Makwana, Y.-T. Duan, U.P. Tarpada, Y.S. Patel, K.B. Patel, V. N. Dave, H.-L. Zhu, Design, synthesis, and antibacterial evaluation of new Schiff's base derivatives bearing nitroimidazole and pyrazole nuclei as potent E. coli FabH inhibitors, Res. Chem. Intermed. 41 (2015) 10137–10149.
[29] O. Gungor, P. Gurkan, Synthesis and characterization of higher amino acid Schiff bases, as monosodium salts and neutral forms. Investigation of the intramolecular hydrogen bonding in all Schiff bases, antibacterial and antifungal activities of neutral forms, J. Mol. Struct. 1074 (2014) 62–70.
[30] K.S. Kumar, S. Ganguly, R. Veerasamy, E. De Clercq, Synthesis, antiviral activity and cytotoxicity evaluation of Schiff bases of some 2-phenyl quinazoline-4 (3) H-ones, Eur. J. Med. Chem. 45 (2010) 5474–5479.
[31] D. Sriram, P. Yogeswari, N.S. Myneedu, V. Saraswat, Abacavir prodrugs: Microwave-assisted synthesis and their evaluation of anti-HIV activities, Bioorg. Med. Chem. Lett. 16 (2006) 2127–2129.
[32] E. Pontiki, D. Hadjipavlou-Litina, A. Chaviara, Evaluation of anti-inflammatory and antioxidant activities of copper (II) Schiff mono-base and copper (II) Schiff base coordination compounds of dien with heterocyclic aldehydes and 2-amino-5-methylthiazole, J. Enzym. Inhib. Med. Chem. 23 (2008) 1011–1017.
[33] P. Rathelot, P. Vanelle, M. Gasquet, F. Delmas, M.P. Crozet, P.J. Timon-David, Maldonado, Synthesis of novel functionalized 5-nitroisoquinolines and evaluation of in vitro Antimalarial activity, Eur. J. Med. Chem. 30 (1995) 503–508.
[34] S. Aggarwal, D. Paliwal, D. Kaushik, G.K. Gupta, A. Kumar, Pyrazole Schiff Base hybrids as anti-malarial agents: Synthesis, in vitro screening and computational study, Comb. Chem. High Throughput Screen. 21 (2018) 194–203.
[35] G. Hu, G. Wang, N. Duan, X. Wen, T. Cao, S. Xie, W. Huang, Design, synthesis and antitumor activities of fluoroquinolone C-3 heterocycles (IV): S-triazole Schiff-Mannich bases derived from ofloxacin, Acta Pharm. Sin. B. 2 (2012) 312–317.
[36] S.M. Bensaber, H. Allafe, N.B. Ermeli, S.B. Mohamed, A.A. Zetrini, S.G. Alsabri, M. Erhuma, A. Hermann, M.I. Jaeda, A.M. Gbaj, Chemical synthesis, molecular modelling, and evaluation of anticancer activity of some pyrazol-3-one Schiff base derivatives, Med. Chem. Res. 23 (2014) 5120–5134.
[37] S.B. Desai, P.B. Desai, K.R. Desai, Synthesis of some Schiff bases, thiazolidinones and azetidinones derived from 2,6-diaminobenzo1,2-d: 4,5-d' bisthiazole and their anticancer activities, Heterocycl. Commun. 7 (2001) 83–90.
[38] S.S. Wazalwar, A.R. Banpurkar, F. Perdih, Synthesis, characterization, molecular docking studies and anticancer activity of Schiff bases derived from 3-(substituted phenyl)-1-phenyl-1H-pyrazole-4-carbaldehyde and 2-aminophenol, J. Chem. Crystallogr. 48 (2018) 185–199.
[39] A.S. Hassan, H.M. Awad, A.A. Magd-El-Din, T.S. Hafez, Synthesis and in vitro antitumor evaluation of novel Schiff bases, Med. Chem. Res. 27 (2018) 915–927.
[40] M.E. Bluhm, M. Ciesielski, H. Gorls, O. Walter, M. Doring, Complexes of Schiff Bases and Intermediates in the Copper-Catalyzed Oxidative Heterocyclization by Atmospheric Oxygen, Inorg. Chem. 42 (2003) 8878–8885.
[41] W.A. Zoubi, Biological Activities of Schiff Bases and Their Complexes: A Review of Recent Works, Int. J. Org. Chem. 03 (03) (2013) 73–95.
[42] I. Król-Starzomska, A. Filarowski, M. Rospenk, A. Koll, S. Melikova, Proton Transfer Equilibria in Schiff Bases with Steric Repulsion, J. Phys. Chem. A. 108 (2004) 2131–2138.
[43] M. I.H. El-Qaliei, S. A.S. Mousa, M.H. Mahross, A.M.A. Hassane, M.A.M. Gad-Elkareem, E.H. Anouar, M. Snoussi, K. Aouadi, A. Kadri. Novel (2-Oxoindolin-3-ylidene)methyl)-1H-pyrazole and their fused derivatives: Design, synthesis, antimicrobial evaluation, DFT, chemical approach, in silico ADME and molecular docking studies. 2022. J. Mol. Struc. 1264, 133299.
[44] A.S. Hassan, A.A. Askar, E.S. Nossier, A.M. Naglah, G.O. Moustafa, M.A. Al-Omar, Antibacterial Evaluation, In Silico Characters and Molecular Docking of Schiff Bases Derived from 5-aminopyrazoles, Molecules 24(17) (2019) E3130.
[45] B.J. Kadhem, J. Alshawi, T.A. Alsalim, M. Abdalla, Novel Schiff Bases Ligands and Their Complexes: Thermal Analysis, Antibacterial Activity, and Molecular Docking, Egypt. J. Chem. 65(7) (2022) 107-119.
[46] P.R. Shetty, G. Shivaraja, G. Krishnaswamy, K. Pruthviraj, V.C. Mohan, S. Sreenivasa, Pyrazole Schiff Bases: Synthesis, Characterization, Biological Screening, In Silico ADME and Molecular Docking Studies, Indian J. Heterocyc. Chem. 30(2) (2020) 123-130.
[47] A.S. Hassan, A.A. Askar, A.M. Naglah, A.A. Almehizia, A. Ragab, Discovery of New Schiff Bases Tethered Pyrazole Moiety: Design, Synthesis, Biological Evaluation, and Molecular Docking Study as Dual Targeting DHFR/DNA Gyrase Inhibitors with Immunomodulatory Activity, Molecules. 25 (11) (2020) 2593.
[48] V.R. Mishra, C.W. Ghanavatkar, S.N. Mali, H.K. Chaudhari, N. Sekar, Schiff base clubbed benzothiazole: synthesis, potent antimicrobial and MCF-7 anticancer activity, DNA cleavage and computational study, J. Biomol. Struct. Dynam. 38 (6) (2020) 1772–1785.
[49] R. Hebbachi, A. Djedouani, S. Kadri, H. Mousser, A. Mousser, 1-[4-({4-[(E)-(2-hydroxynaphthalen-1-yl)methylideneamino]phenyl}sulfanyl)-phenyl]ethanone, Acta Cryst. E69 (2013) o67–o68.
[50] R. Hebbachi, A. Djedouani, S. Kadri, H. Mousser, A. Mousser, Crystal structure of (E)-1-[4-({4-[(4-methoxybenzylidene)amino]phenyl}sulfanyl)phenyl]ethan-1-one, Acta Cryst. 71 (2) (2015) o109–o110.
[51] M. J. Frisch, G. W. Trucks, H. B. Schlegel, et al., Gaussian 09, Revision A.1, Gaussian Inc., Wallingford, CT, 2009.
[52] https://cccbdb.nist.gov/vibscalejust.asp.
[53] R. Dennington, T. Keith, J. Millam, Semichem Inc, Shawnee Mission, KS, 2009.
[54] M. Turner, J. McKinnon, S. Wolff, D. Grimwood, P.D.J. Spackman, M. Spackman, CrystalExplorer17, University of Western Australia, 2017.
[55] G.M. Morris, R. Huey, W. Lindstrom, M.F. Sanner, R.K. Belew, D.S. Goodsell, A. J. Olson, Autodock4 and AutoDockTools4: automated docking with selective receptor flexiblity, J. Comput. Chem. 2009 (16) (2009) 2785–2791.
[56] H.M. Berman, J. Westbrook, Z. Feng, G. Gilliland, T.N. Bhat, H. Weissig, I. N. Shindyalov, P.E. Bourne, Nucleic Acids Res. 28 (1) (2000) 235–242, https://doi.org/10.1093/nar/28.1.235. (http://www.rcsb.org).
[57] X. Qiu, C.A. Janson, W.W. Smith, S.M. Green, P. McDevitt, K. Johanson, P. Carter, M. Hibbs, C. Lewis, A. Chalker, A. Fosberry, J. Lalonde, J. Berge, P. Brown, C.S. V. Houge-Frydrych, R.L. Jarvest, Crystal structure of Staphylococcus aureus tyrosyl-tRNA synthetase in complex with a class of potent and specific inhibitors, Protein Sci. 10 (10) (2001) 2008–2016.
[58] D.B. Bax, P.F. Chan, D.S. Eggleston, A. Fosberry, D.R. Gentry, F. Gorrec, I. Giordano, M. Hann, A. Hennessy, M. Hibbs, J. Huang, E. Jones, J. Jones, K. K. Brown, C.J. Lewis, E.W. May, M.R. Saunders, O. Singh, C.S. Spitzfaden, C. Shen, A. Shillings, A.F. Theobald, A. Wohlkonig, N.D. Pearson, M.N. Gwynn, Type II A topoisomerase inhibition by a new class of antibac-terial agents, Nature. 466 (2010) 935–940.
[59] T.D. Goddard, C.C. Huang, T.E. Ferrin, Visualizing density maps with UCSF Chimera, J. Struct. Biol. 157 (2007) 281–287.
[60] J. Bernstein, R.E. Davis, L. Shimoni, N.L. Chang, Patterns in Hydrogen Bonding: Functionality and Graph Set Analysis in Crystals, Angew. Chem. Int. Ed. Engl. 34 (15) (1995) 1555–1573, https://doi.org/10.1002/anie.199515551.
[61] J. Klocker, A. Karpfen, P. Wolschann, Surprisingly regular structure–property relationships between C-O bond distances and methoxy group torsional potentials: An ab initio and density functional study, J. Mol. Struct. 635 (2003) 141–150.
[62] P.Y. Ayala, G.E. Scuseria, Linear scaling second-order Moller-Plesset theory in the atomic orbital basis for large molecular systems, J. Chem. Phys. 110 (1999) 3660.
[63] C. Parlak, Ö. Alver, C. Naphtaly M. Ouma, L. Rhyman & Ponnadurai Ramasami. Interaction between favipiravir and hydroxychloroquine and their combined drug assessment: in silico investigations, Chem. Pap. 76 (2022) 1471–1478.
[64] C. Parlak, Ö. Alver, C. N. M. Ouma, L. Rhyman, P. Ramasami. Can the Antivirals Remdesivir and Favipiravir Work Better Jointly? In Silico Insights, Drug Res (Stuttg). 72(1) (2022) 34-40.
[65] J. Kawakami, H. Kakinami, N. Matsushima, A. Nakane, H. Kitahara, M. Nagaki, S. Ito, Structure–activity Relationship Analysis for Antimicrobial Activities of Tryptanthrin Derivatives Using Quantum Chemical Calculations, J. Comput. Chem. Jpn. 12 (2) (2013) 109–112.
[66] J.J. McKinnon, M.A. Spackman, A.S. Mitchell, Novel tools for visualizing and exploring intermolecular interactions in molecular crystals, Acta Crystallogr. 60B (2004) 627–668.
[67] H.C. Jubb, A.P. Higueruelo, B. Ochoa-Montaño, W.R. Pitt, D.B. Ascher, T. L. Blundell, Arpeggio: A Web Server for Calculating and Visualising Interatomic Interactions in Protein Structures, J. Mol. Biol. 429 (2016) 365–371.
[68] A.C. Wallace, R.A. Laskowski, J.M. Thornton, LIGPLOT: a program to generate schematic diagrams of protein-ligand interactions, Protein Eng. 8 (1996) 127–134. LIGPLOT vol 4.5.3.
[69] K. Stierand, P.C. Maass, M. Rarey, Molecular complexes at a glance: automated generation of two-dimensional complex diagrams, Bioinformatics 22 (14) (2006) 1710–1716, https://doi.org/10.1093/bioinformatics/btl150.
[70] P.C. Fricker, M. Gastreich, M. Rarey, Automated drawing of structural molecular formulas under constraints, J. Chem. Inf. Comput. Sci. 44 (3) (2004) 1065–1078, https://doi.org/10.1021/ci049958u.